Ice Dynamics of Union glacier (Antarctica) by means of SAR data

Rodrigo Gómez Fell

Dissertação de Mestrado apresentada ao Programa de Pós-graduação em Oceanografia Física, Química e Geológica do Instituto de Oceanografia da Universidade Federal do Rio Grande, como parte dos requisitos para obtenção de título de Mestre.

Orientador: Prof. Dr. Jorge Arigony-Neto

Co-orientador: Dra. Angela De Santis

Rio Grande
Março de 2018

Ice Dynamics of Union glacier (Antarctica) by means of SAR data

Rodrigo Gomez Fell

Dissertação de Mestrado aprovada em _____ de _____ de 2018 pela banca examinadora composta pelos seguintes membros:

Prof. Dr. Jorge Arigony-Neto (orientador) . . . . IO/FURG

Prof. Dr. Jefferson Simões . . . . IGEO/UFRGS

Prof. Dr. Maurício Mata . . . . IO/FURG

Profª Drª Juliana Costi . . . . IMEF/FURG

Prof. Dr. Fabrício Oliveira . . . . IO/FURG

Com amor para:

Andrea, Margarita y Salvador.

"Every day some new fact comes to light - some new obstacle which threatens the gravest obstruction. I suppose this is the reason which makes the game so well worth playing."

Captain Robert Falcon Scott

Agradecimentos

Resumo

É previsto que o manto de gelo da Antártica seja o principal contribuinte para o aumento do nível do mar durante o século XXI. Portanto, o monitoramento da dinâmica do gelo de suas geleiras de descarga é de grande importância para estimar futuras previsões do aumento do nível do mar. Usando técnicas de sensoriamento remoto, combinadas com medições de campo é possível obter uma boa aproximação de sua dinâmica e esta informação ser utilizada como entrada para modelagem glacial. A Geleira Union é uma das principais geleiras de descarga da cadeia de montanhas Ellsworth, Antártica Ocidental, e sua massa de gelo alimenta a plataforma de gelo de Ronne-Filchner. A Geleira Union apresenta sua linha de encalhe abaixo do nível do mar e com um perfil topográfico invertido, caracterizando-a sensível às futuras mudanças na estabilidade da Plataforma de Gelo de Ronne-Filchner. Velocidades de fluxo superficial foram calculadas a partir de imagens SAR Stripmap HIMAGE COSMO-SkyMed do verão austral de 2011-2012 aplicando-se a técnica de offset tracking. Os resultados foram comparados com dados de campo obtidos com GPS diferencial. Foi estimada uma velocidade média de 0.043 (0.0393 SD) $\mathrm{m\,d^{-1}}$ para o vale principal, com valores máximo de $0.325\,\mathrm{m\,d^{-1}}$. Um modelo de espessura do gelo foi proposto com base na teoria de fluxo laminar utilizando-se a velocidade superficial combinada com valores de inclinação do terreno, derivada do modelo de elevação TanDEM-X. A espessura do gelo modelada foi comparada com 4107 pontos de radar de penetração de solo (GPR) e apresentou concordância com um desvio médio absoluto de 21.28%. Por fim, taxas de deformação do gelo foram calculadas e relacionadas às características superficiais, e.g. fendas, visíveis em imagens COSMO-SkyMed Spotlight-2 de altíssima resolução. As magnitudes das taxa de deformação podem ser associadas e explicar o ciclo de abertura e fechamento das fendas. Obteve-se magnitudes máximas de $-0.078\,\mathrm{a^{-1}}$ e $0.039\,\mathrm{a^{-1}}$ para as forças de tensão de compressão e de extensão, respectivamente.

Palavras-chave: Sensoriamento Remoto;correlação cruzada; Dados satélitais SAR; Antártica; Geleira Union; dinâmica do gelo; modelagem da espessura do gelo; Taxas de deformação da geleira, fendas do gelo.

Abstract

The Antarctic ice sheet is predicted to be the major contributor to sea-level rise during the XXI century. Therefore, monitoring ice dynamics of outlet glaciers in Antarctica is of great importance to assess future sea-level rise predictions. Glaciers can be studied using remote-sensing techniques, which combined with field measurements can deliver a good approximation of its dynamics, which can be used as input for glacier models. Union Glacier is one of the major outlet glaciers of the Ellsworth Mountains and drains into the Ronne-Filchner Ice Shelf. The grounding line of Union glacier is below sea level and is on a reverse slope, making Union glacier sensible to future changes over the Ronne-Filchner ice shelf. In this study we acquired high resolution Stripmap HIMAGE SAR images from the COSMO-SkyMed satellite constellation during austral summer of 2011-2012, and applied SAR offset tracking to compute ice velocities. Then, we compared our derived velocities with field data. Mean values of ice velocity estimated for the main trunk of the glacier are 0.043 (0.0393 SD) $\mathrm{m\,d^{-1}}$, with values reaching up to $0.325\,\mathrm{m\,d^{-1}}$, in agreement with previous studies. A model of ice thickness based on lamellar flow theory is proposed, using estimated surface ice velocity in combination with surface slope derived from TanDEM-X as input data. Comparison of our modeled ice thickness with radar data agree with a mean absolute deviation of 21.28%. Strain rates magnitudes can be associated with crevasse life-cycles. We computed principal strain rates from surface ice velocities in order to assess crevasse formation and closure. We found maximum magnitudes values for the principal-strain rates axes of $-0.078\,\mathrm{a^{-1}}$ and $0.039\,\mathrm{a^{-1}}$, for compression and extension respectively, over selected areas. Thereafter, using high resolution COSMO-SkyMed Spotlight-2 SAR images we establish a relation between surface features and acting strain components.

Keywords: Remote Sensing, SAR offset tracking, Antarctica, Union Glacier, ice thickness model, ice dynamics, glacier strain rates, crevasses.

Contents

List of Figures

List of Tables

List of Symbols and Acronyms

τ_b	Basal drag
τ_d	Driving stress
g	Gravitational acceleration; $(9.8\,\mathrm{m\,s^{-1}})$
C	Error of the tracking algorithm
Δt	Time span between image acquisitions
Δx	Pixel resolution in ground range
α	Glacier slope
$\dot{\varepsilon}$	Shear strain rate
ρ	Ice density; $(917\,\mathrm{kg\,m^{-3}})$
e_t	Uncertainties of the ice velocity model
z	Oversampling factor
A	Glen's law creep parameter
AIS	Antarctic Ice Sheet
CSK	Cosmo-SkyMED
GPR	Ground Penetrating Radar
H	Ice thickness
IPCC	Intergovernmental Panel on Climate Change
MEaSUREs	Making Earth System Data Records for Use in Research Environments
MISI	Marine Ice Sheet Instability
n	Glen's law creep exponent
SAR	Synthetic Aperture Radar
WAIS	West Antarctic Ice Sheet

Chapter 1

Introduction

Glacier masses act as water reservoirs, altering the level of oceans and consequently changing continental coast lines. Antarctic and Greenland Ice Sheets are bound to be the principal contributors to sea level rise in the XXI century, mainly due to accelerated mass loss (Rignot et al., 2011b). Their contribution will be more important than ice caps, mountain glaciers or thermal expansion of the oceans (Cazenave et al., 2008; Dutton et al., 2015).

The fifth Intergovernmental Panel on Climate Change (IPCC) states with high confidence that the rate of sea level rise since the mid XIX century is higher that the mean rate of the last two millennia and that during the last hundred years it has rise by 0.19 ± 2 m and will continue to rise during the XXI century (Church et al., 2013). New estimates of sea level rise acceleration states, that at the current rate will more than double the mean sea level estimations for 2100, with the current rate unchanged and without taking into account rapid ice sheet dynamic changes (Nerem et al., 2018).

Antarctic Ice Sheet (AIS) is the world's largest fresh water reservoir with an area of 13.5 million km^2 and a volume of 25.4 million km^3 (Benn et al., 2010). The ice sheet is divided in East and West by the Trans Antarctic Mountains. East Antarctica Ice Sheet being larger in extent than West Antarctic Ice Sheet (WAIS), with precipitation and ablation regimes being different in this two areas (Turner et al., 2014).

One of the biggest concerns about Antarctica is the collapse of ice shelves around the

continent (Rignot et al., 2004; Scambos et al., 2004; Rignot et al., 2013; Hellmer et al., 2017) and marine ice shelf instability (MISI) of the WAIS (Rignot and Jacobs, 2002; Nicholls et al., 2009; Ross et al., 2012; Purkey and Johnson, 2013). Bamber et al. (2009) estimated that the mass loss of only WAIS due to MISI has the potential to contribute 3.3 m of sea-level rise.
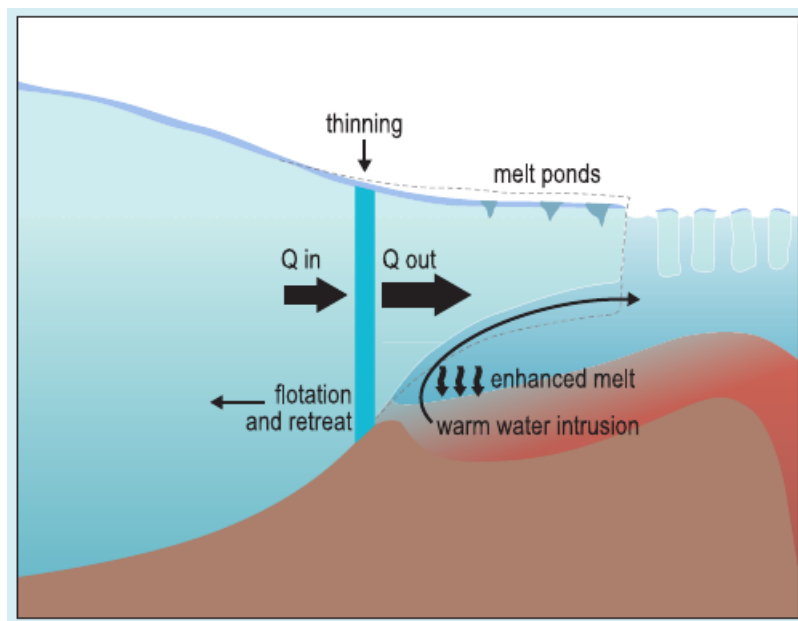
Figure 1.1: Schematic representation of the marine ice shelf instability process with a reverse slope component. Where the warm water intrusion enhance basal melt causing a debilitation of the ice shelve with a consequent glacier thinning due to augmenting glacier ice flux (Q), producing a self sustained grounding line retreat. Modified from Church et al. (2013).

The warming of the atmosphere has augmented the ocean temperature (Stocker et al., 2015), and waters around Antarctica are no exception (Schmidtko et al., 2014; Jacobs et al., 2011). This warm up has brought changes in circulation with further incursions of shelf water onto the continental shelf (Jacobs et al., 2011). Increasing basal melting of ice shelves (Pritchard et al., 2012) had developed an ice shelf thinning with potential fracture and collapse of the ice shelf (Shepherd et al., 2004), removing ice shelf buttressing with a consequent glacier acceleration of the ice and thinning plus a migration of the grounding line. Grounding line is the boundary where the ice starts to float and leaves anchored

ground (Schoof, 2007). Buttressing is the force that exerts the ice shelf over the outlet discharge glaciers, hence regulating their flow.
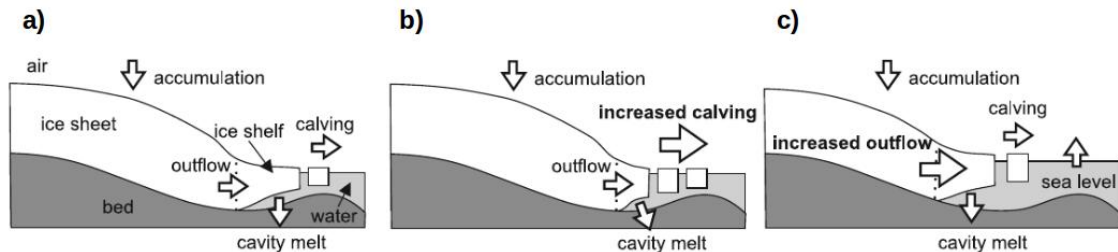
Figure 1.2: Main components of mass balance of a marine ice sheet. (a) Increase cavity melt leads to, (b) increase calving and eventually to an (c) increased outflow of the ice sheet, hence affecting sea level. Modified from Schoof (2007).

The MISI hypothesis states that when this migration occurs over a reverse slope, that descends in the direction of the retreat, the grounding line can move rapidly and in a self sustained pace further inland, leaving extensive portions of the glacier floating. Therefore, eventually will have further basal melting and thinning due to a warming ocean and the MISI cycle would repeat until the glacier founds a positive slope to anchor (Mercer, 1978; Joughin and Alley, 2011; Ross et al., 2012). A simplification of the MISI processes is presented on figure 1.1.

The two main mechanisms that dominate glacier mass loss over the Antarctic continent are basal melt and ice front calving (Depoorter et al., 2013; Rignot et al., 2013; Pauling et al., 2016). This processes when , intensified, are considered as the prime reasons for reduced buttressing and increased glacier flow, affecting glacier ice dynamics (Rignot et al., 2011b, 2013; Schmidtko et al., 2014). Figure 1.2 shows this cycle of increase cavity melt and calving leading to increasing outflow.

Over this work we used satellite synthetic aperture radar (SAR) data to obtain surface ice velocities of an outlet glacier in West Antarctica. This velocities are then used to infer ice thickness, hence volume, of the glacier and principal strain rates to asses crevasse formation. This information can help us understand ice dynamic processes over Union

glacier.

Surface ice velocities obtained with satellite data are a valuable tool to assess ice dynamics over remote and vast environments (eg., Morlighem et al. 2011; Fitzpatrick et al. 2013; Osmanoglu et al. 2014). This technique has being used extensively in cryospheric studies since the last decade of the Twentieth century (eg., Scambos et al. 1992; Fahnestock et al. 1993; Rosanova et al. 1998). Monitoring changes in surface ice velocity over time can be an indicator of how glaciers are affected by climate (Pellikka and Rees, 2010), and be used as input for modeling different parameters of glacier dynamics (eg., Young and Hyland 2002; Rankl et al. 2017).

We calculate high resolution surface ice velocity fields for Union glacier. The ice velocity measurements were used to model glacier ice thickness and study surface strain rates over the glacier. Ice volume, mass and the sea level equivalent of Union glacier was calculated from a complete ice thickness model derived from the Making Earth System Data Records for Use in Research Environments (MEaSUREs) ice velocity data set.

The thickness of a cold base glacier influences directly its dynamics, with creep by deformation being is driver, and thus depending on topographic constrains of the glacier (eg. rock margins, slope, bedrock promontories). For example, the higher the slope, the thinner the glacier would be over that area (Nye, 1952a).

Accurate estimates of ice thickness are hard to obtain. Methods based on airborne or ground penetrating radar (Fischer, 2009) and active seismology (Peters et al., 2008) are excellent tools to get field measures. However, they are normally constrained to a small area, because they are quite expensive to be used for large areas. On the other hand, modeling based on derived variables can approximate ice thickness with high accuracy (eg., McNabb et al. 2012; Farinotti et al. 2013; Gantayat et al. 2014). This is specially true if glacier thickness field data is available, giving the possibility of accurate model calibration (Farinotti et al., 2009). We follow lamellar flow theory to model ice thickness of Union Glacier (Gantayat et al., 2014), combined with ground penetrating radar (GPR)

data for calibration and validation.

Strain rates can be computed from ice surface velocity data derived from satellite remote sensing (eg., Young and Hyland 2002; Rankl et al. 2017). They have been used to assess ice shelf stability and fracture (Rankl et al., 2017), study spatial distribution of transverse and longitudinal strain rates over ice shelfs (Young and Hyland, 2002), find a relation between moulins, crevasses and altitude (Poinar et al., 2015), and for calculate tensile stresses for identification of surface crevassed areas (LeDoux et al., 2017). In this study we use strain rates in order to relate them to crevasse formation and ice flow dynamics over the surface of the glacier.

Using surface ice velocities obtained by remote-sensing techniques, we model ice thickness and strain rates; in order to understand Union glacier ice dynamics, its driving factors and implications on glacier surface features.

1.1 Motivation

The first scientific expedition to Union Glacier was conducted by the US Geological Survey during the summer of 1962/63. Then an airborne survey by the British Antarctic Survey was carried out in 1974/75. Since then and prior of the establishment of the blue ice airstrip, only one expedition was conducted in 2007 over the area (Rivera et al., 2010). After the establishment of the airstrip as a base for the company Antarctic Logistics and Expeditions (ALE), four glaciological campaigns where conducted between 2008 and 2011 (Rivera et al., 2014b,a). Since the year 2011 a Brazilian- Chilean program was established with the joint cooperation between the INCT da Criosfera and INACH to study the area and its surroundings. Since the 2010 ALE base establishment and the 2014 inauguration of the Chilean base "Estacion Polar Cientifica Conjunta" more scientific programs have been set on the glacier. Programs that are from a wide range of disciplines and scientific interest from measurement of snow and ice albedo (Cordero et al., 2014), geo-

morphology (Costa et al., 2017) or extremophiles yeasts (Barahona et al., 2016), making Union Glacier an interesting scientific gateway to inland Antarctica.

Rivera et al. (2010) give the first estimations of mass balance and measurements of surface and sub-glacial topography. They suggested that Union Glacier is in a near-equilibrium state, based in an mass balance ice-flux model, that estimates a net mass balance of $0.18 \pm 0.05\,\mathrm{m\,a^{-1}}$. This estimate was based assuming that the glacier is in an equilibrium state. Also mean ice thickness of $1450\,\mathrm{m}$ was measured in a section of the glacier.

A more complete glaciological description was made for the area by Rivera et al. (2014b), with the aim to develop a baseline for future studies. Glacier velocity was estimated using 27 bamboo stakes measured between 2007 and 2011. The glacier velocity was found to be between $0.1\,\mathrm{m\,a^{-1}}$ to $34.6\,\mathrm{m\,a^{-1}}$, with a mean velocity at the gate area of $20\,\mathrm{m\,a^{-1}}$. The gate area is defined as the narrower flow path over the glacier. Moreover, velocities were found to increase downstream of the gate and the maximum velocity was observed at the steepest area of Union glacier main valley. A radar survey was carried out, yielding a sub-glacial topography below sea level ($-858\,\mathrm{m}$) and a maximum altitude of $-190\,\mathrm{m}$ between the gate and the grounding line zone. Finally no seasonal or tidal modulated variations were detected.

An important characteristic in the evolution of glaciers is their flow and deformation (Pellikka and Rees, 2010). Glaciers and ice streams dynamics flowing into the Ronne-Filchner ice shelf are largely unknown, mainly because of the lack of survey data (Bingham et al., 2015), monitoring changes at Union Glacier through time will give glaciological information about the glacier and the ice shelf bound to it.

SAR satellite remote sensing is an excellent tool for monitoring remote locations, where in-situ monitoring its hard or sometimes unthinkable, and in areas like Antarctica where clear skies are rare, and half of the year sunlight is absent (Pellikka and Rees, 2010).

The ice velocity measurements available for Union glacier are either sparse over space or of low resolution. Hence, a detailed high resolution map of superficial ice velocities for Union Glacier has not been done and is needed. The only spatial measurements of ice velocities published are in Rivera et al. (2010, 2014b) and the ones that are part of a compilation for the whole continent (Fahnestock et al., 2016; Rignot et al., 2017), with a scale on the order of hundreds of meters. These measurements are a good base for monitoring and assess the conditions of ice sheet stability, but more detailed high resolution data regarding ice velocities will give a better estimation of ice dynamics of outlet glaciers constraint by an ice shelf as is Union glacier (Benn et al., 2010).

The Ground Penetrating Radar (GPR) ice thickness measurements (Rivera et al., 2014a) compared to BEDMAP2 model (Fretwell et al., 2013) showed an important difference over Union Glacier. Consequently, a full ice thickness model estimation of the glacier is proposed.

Even do satellite imagery is widely used in glaciological studies, glacier strain rates studies from satellite data are not that usual and they are mostly focus over ice shelves due to its inherent dynamics (eg,. Young and Hyland 2002; Rankl et al. 2017). Stress and strains can help us understand how a glacier flow and deform. Stress is linked with downslope flow and strain rate is the deformation effect of that stress over a period of time. Hence, that effect is to deform (strain) and creep (flow). Moreover, shifts over time or space on strain rates can be considered of sign of a changing glacier (Cuffey and Paterson, 2010).

Finally, the study area has been part of the joint work between Instituto Anatartico Chileno (INACH) and Laboratorio de Monitoramento da Criosfera (LaCrio/FURG) that is being done over Union Glacier since 2011. Making the area a natural laboratory for research, with relatively easy access, gives the possibility to study the interior of Antarctica, accumulation areas, grounding line zones, ice dynamics, tidal effect on glaciers and other processes and features that occurs in deep Antarctica behind the big ice shelf of

Ronne-Filchner.

1.2 Study Area

Union Glacier is located in the West Antarctic Ice Sheet, in the southern part of the Ellsworth Mountains, Heritage Range area (79°46′S, 83°24′W). It is one of the major outlet glaciers of the Heritage Range and its basin drains into the Constellation Inlet, part of the Ronne-Filchner Ice Shelf (Figure 1.3).
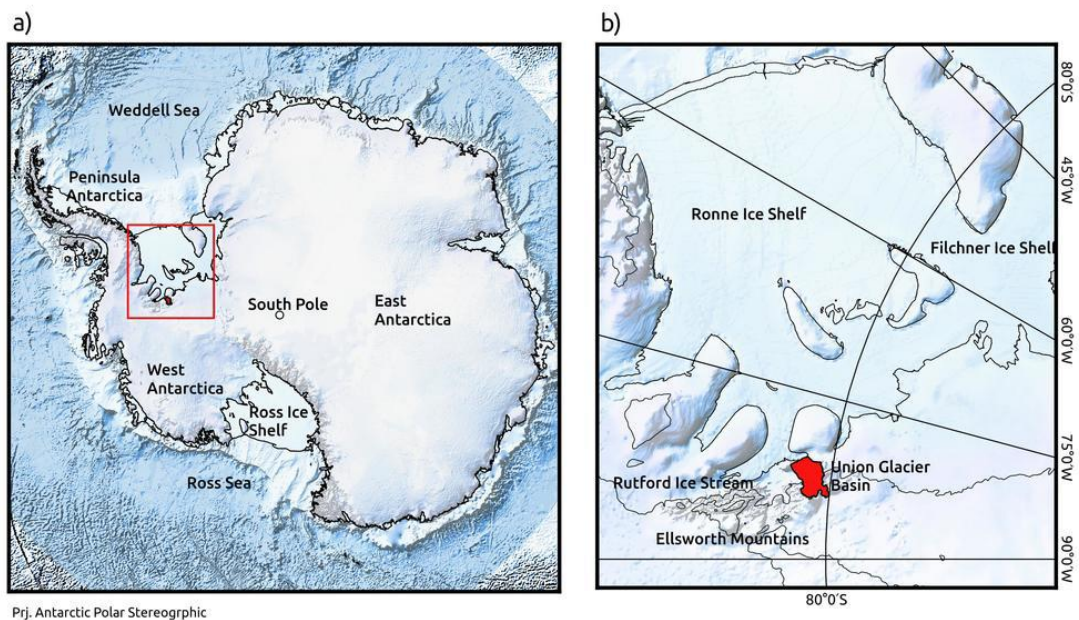
Figure 1.3: a) Antarctic continent with main features highlighted. b) Union glacier basin (red) and is geographical setting.

Ronne-Filchner Ice Shelf is located south of the Weddell Sea, east of the Antarctic Peninsula, and is composed of two separated areas: the Filchner sector to the east and the Ronne sector closer to the Antarctic Peninsula. It is the second biggest ice shelf of Antarctica ($443\,140\,\text{km}^2$). The platform is loosing $115.4 \pm 45\,\text{Gt}\,\text{a}^{-1}$ via basal melting (Rignot et al., 2013) and there is a concern about the potential collapse of the platform because of warming of the oceans during the XXI century (Hellmer et al., 2012, 2017).

Union Glacier has a total length of 86 km from the Institute Ice Stream divide to its grounding line at Constellation Inlet, with an estimated surface area of $2561\,km^2$ (Rivera et al., 2010). The glacier valley is oriented southwest - northeast with several smaller glacier tributaries draining into it. There is a narrow cross-section (7 km wide) or flux gate, where the entire mass flowing from the plateau has to go through (Rivera et al., 2014b).

There are two heavily crevassed areas along the main trunk, first when Schanz glacier joins with the main Union trunk (Figure 1.4) and a second one 41 km from the grounding line, associated with a change in relief. This crevasse field was mapped in detail with GPR in Figure 31.8 by Rivera et al. (2014a). Other crevassed areas are along the sides of the fastest flowing part of the glacier.
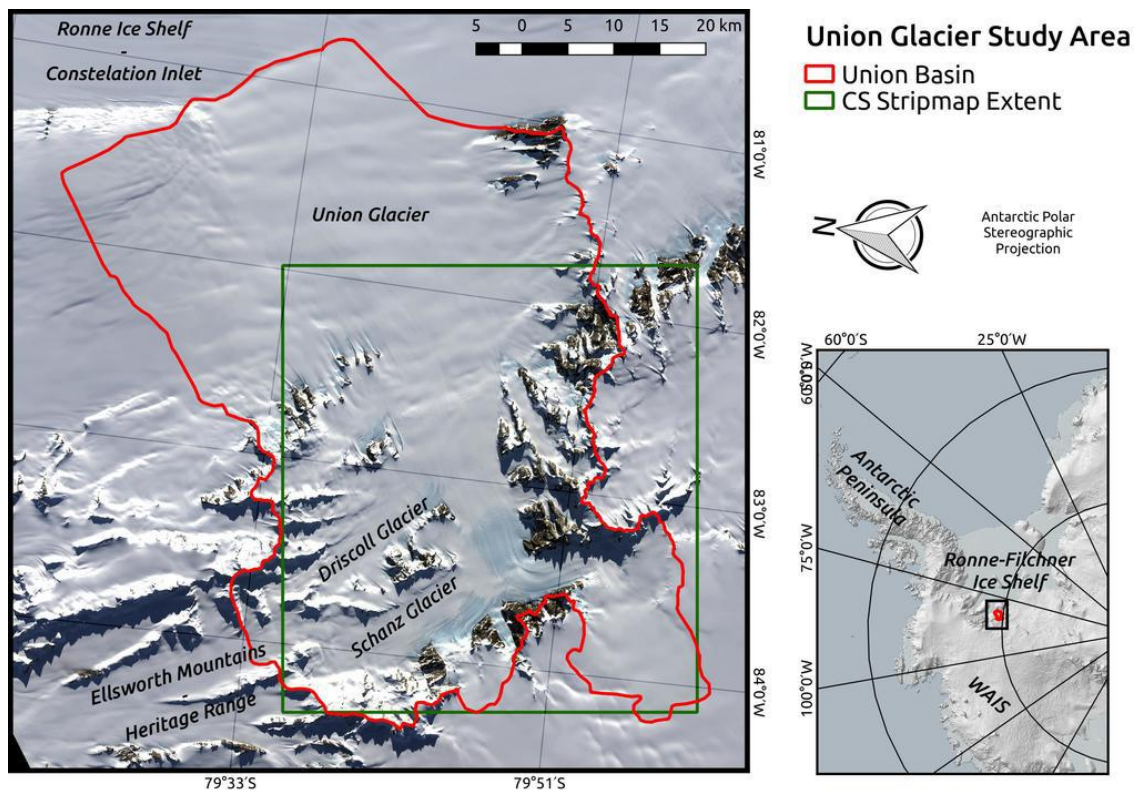
Figure 1.4: Union glacier basin with the footprints of SAR images used in the study. Green polygon show the geographical coverage of Cosmo-SkyMED Stripmap data. Background image is a Landsat-8 scene in true color RGB (432).

1.3 Objectives

1.3.1 Main Objective

The main objective of this work is to characterize ice dynamic parameters of Union Glacier, a remote and strongly buttressed glacier in Antarctica, based on surface ice velocity fields obtained with remote sensing techniques.

1.3.2 Specific Objectives

Secondary objectives of the thesis are:

- To extract and validate ice flow velocities from satellite radar images;
- To use the ice flow velocities data in a model to estimate the ice thickness and infer ice volume of Union Glacier; and
- To relate surface crevasse formation processes in 3 selected areas of the Union Glacier with glacier strain rates estimated from glacier surface velocities.

Chapter 2

Theory and data

2.1 Ice dynamics

Glaciers slide down slope because of the gravity forces exerted over the ice mass. Snow is accumulated on the upper areas of a glacier due to precipitation and windblown snow (mass gain). Thereafter, snow is compacted into ice as a result of the pressure of the overlying layers of snow. The accumulated mass flows downslope because of its own weight. Ice is removed (mass loss) from the lower parts of a glacier by ablation or a combination of ablation and calving for marine or lake terminating glaciers. A glacier is in a steady state when mass gain by accumulation equals mass loss by ablation (ablation plus calving). The line dividing the areas of accumulation and ablation is called the equilibrium line. In polar regions, where there is not mass loss by ablation the equilibrium line is closer to the marine glacier terminus or sometimes is the terminus (Benn et al., 2010).

On figure 2.1 two different representations of a glacier flow are shown, one a valley glacier and the other a polar ice cap or ice sheet. Areas of accumulation and ablation are well defined. The effect of gravity can be notices as the flow lines move from the upper part of the glacier to the terminus. Note that the graph shows an equilibrium state where the specific net budget (accumulation - ablation) equals zero.There is difference between accumulation and ablation zones, with a greater accumulation area on polar glaciers. Glaciers outside polar regions are sustained either by high solid precipitation or
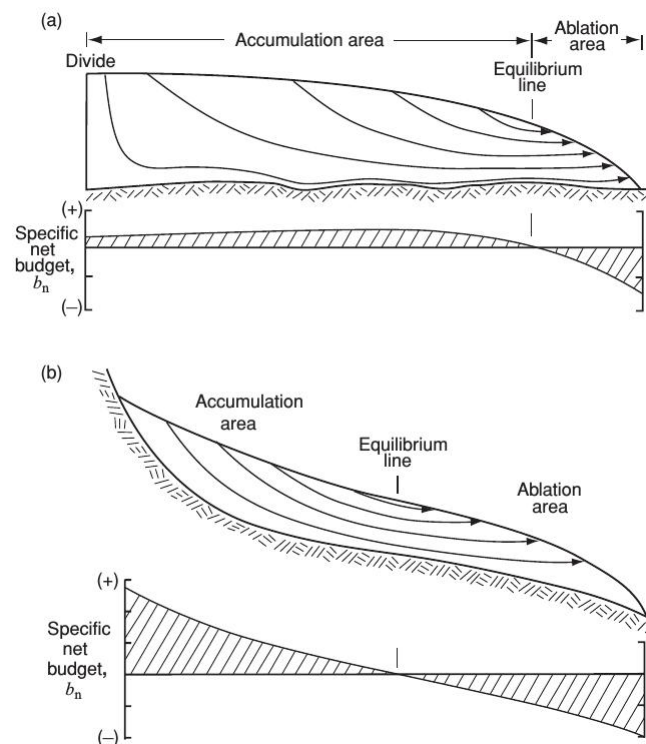
Figure 2.1: Representations of equilibrium line and flow lines on a) polar ice cap or ice sheet and b) valley glacier. Modified from Hooke (2005)

high altitude, where solid winter precipitation exceeds summer melt over the accumulation area. Polar ice sheet experience lower temperatures but less snow precipitation, being calving or melting of their marine terminus the main mass loss Hooke (2005); Benn et al. (2010).

Glacier ice flow is driven by gravitational forces acting on a slope and is controlled by different factors like valley geometry (eg., slope, valley width), ice thickness, mass balance, ice temperature, ice density, termination environment, bedrock or sub glacial hydrology (Cuffey and Paterson, 2010). The simplest model representation of the flowing of ice would be an ice slab over an inclined plane (figure 2.2a), this is called a lamellar ice model (Nye, 1952b; Van der Veen, 2013), where the velocity varies from the surface to the bottom. All glaciers flow because of the creep of ice and some of them also by basal sliding, this depends on the environment where the glacier is located and the type of bedrock that is beneath the ice. A third possible component that can help ice flow is sub-

glacial deformation, when the till at the bottom of a glacier are too soft they can deform pushing the glacier froward (Benn et al., 2010).

We can consider that a glacier is in equilibrium of forces at a given moment in time. Hence gravitational driving forces would be balanced by resisting stresses. On figure 2.2b, the downslope component of weight is resisted by the driving stress (τ_d) over the ice column and basal drag or shear stress (τ_d) at the ice-rock interaction boundary. Other resisting stresses not represented here are for example lateral drag as a result of valley walls. Sometimes this stresses can be neglected. In the case of ice shelfs, basal drag can be assume zero and in ice sheets that are very wide the effect of lateral drag can be ignored (Cuffey and Paterson, 2010).
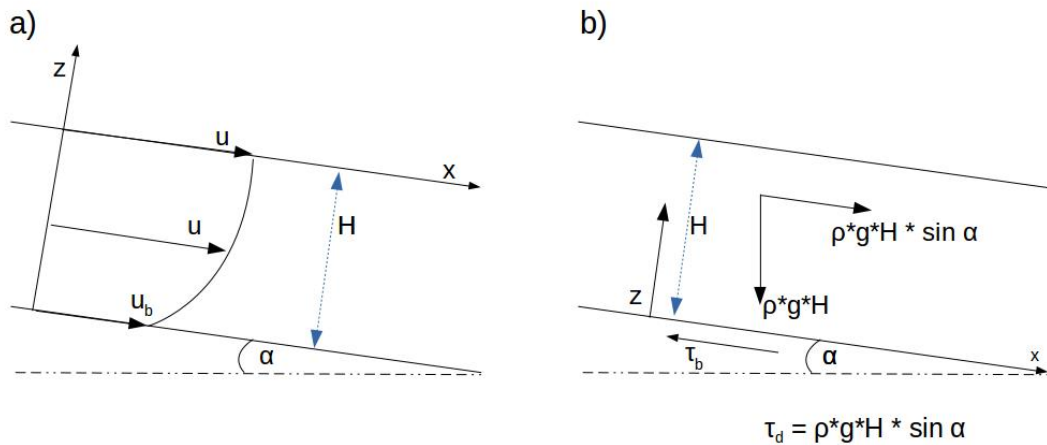
Figure 2.2: Representation of a lamellar ice model over a inclined plane with (α) degree slope. a) Shows the relation between surface velocity (U_s) and basal velocity (U_b) , modified from (Nye, 1952b) and b) Down slope component of weight as a gravitational force of driving stress, modified from (Cuffey and Paterson, 2010). Where H is ice thickness, τ_d is the driving stress, τ_d is the basal stress, ρ is the ice density, g is the gravitational acceleration, and z and x are the vertical and zonal axes.

The effect that stress has over ice when it flows is to deform it. We call this deformation strain. Longitudinal and compressional stresses over ice due to the acceleration (i.e., tensile stress) or deceleration (i.e., compressive stress). The relation between stress

a)

b)
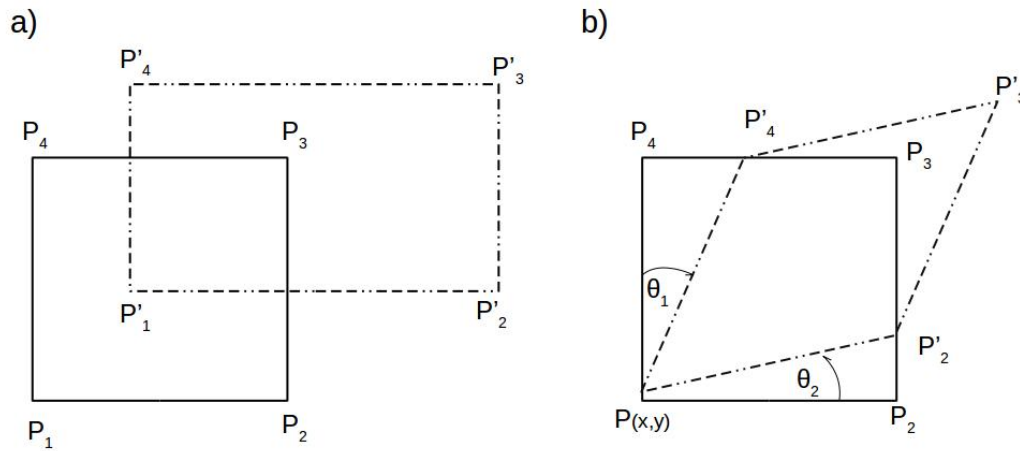
Figure 2.3: Deformation on the two-dimensional plane. a) Normal strain, with extension and/or compression deformations. b) Shear strain changes the angular shape of an element. Modified from (Cuffey and Paterson, 2010)

and strain is given by the so called Glens Law. This flow law of ice is based in laboratory experiments done by John Glen (Glen, 1955). The empirical flow law for ice in steady state ice creep is written as:

$$\dot{\varepsilon} = A\tau^n \tag{2.1}$$

Where $\dot{\varepsilon}$ is the shear strain rate, τ is the applied stress, n is the creep exponent and A is the viscosity or so called softness parameter (Hooke, 2005). Glens relation gave a frame between movement by creep (deformation) and applied stress. When the stress exceeds a certain threshold a failure of the material occurs. This is the yield stress. Crevasses are an example of permanent deformation of the ice. Deformations are a combination of extension, contraction and shear. When extension or contraction deformations occurs is called a normal strain (Figure 2.3a), and when it changes in an angular shape we call it shear strain (Figure 2.3b). In general shear not only deforms but also rotates. Strain rates can be seen as displacements, for example the deformation between P_1 and P_1' can

be express as the vector $\overrightarrow{P_1P_1'}$ (Cuffey and Paterson, 2010).

We can found for strains a set of principal axes that are normal to the stress made. We called them principal strains, and use them in order to asses crevasse formation over an area.

2.2 Satellite SAR Data

The data used here was obtained from two different satellite missions: Constellation of Small Satellites for Mediterranean basin Observation (Cosmo-SkyMED) of the Italian Aerospace Agency (ASI) and TerraSAR-X add-on for Digital Elevation Measurements (TanDEM-X) from the German Aerospace Center (DLR) and ground data collected by Chilean research center Centro de Estudios Cientificos (CECS).

2.2.1 Synthetic Aperture Radar (SAR)

Satellite remote sensing can be classified in two broad categories, passive and active sensors. Passive sensors capture the Sun energy reflected or emitted by the Earth's surface in different wavelengths. Active sensors on the other hand, use an artificial energy pulse that is emitted by an antenna mounted on the satellite, energy reflected by the earth surface is then recorded by the satellite sensor. Active satellites can operate day and night in almost all weather conditions. On the contrary, passive sensors depend on the Sun and proper atmospheric conditions (Pellikka and Rees, 2010).

Synthetic aperture radars (SAR) have active sensors that emit a microwave pulse with a frequency ranging between 0.3 GHz to 40 GHz. The most common bands used by SAR satellites are L-band (1 to 2 GHz), C-band (4 to 8 GHz) and X-band (8 to 12.5 GHz). The energy reflected by a target, or backscattering, depends largely on the frequency and wavelength of the emitted pulse, the properties of the surface (eg., slope, roughness, density) and how the pulse is reflected, scattered, absorbed and/or transmitted by the

object (Pellikka and Rees, 2010).
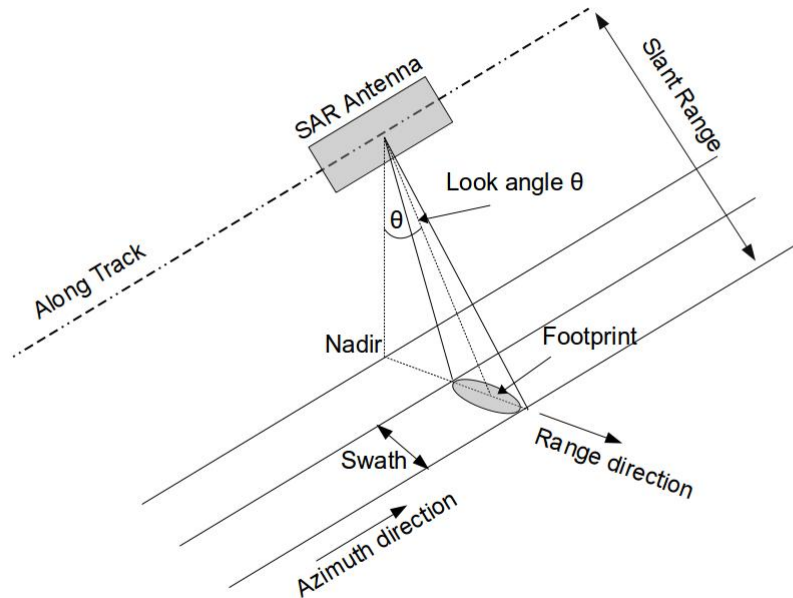
Figure 2.4: Simplified SAR geometry of data acquisition. Left side configuration antenna with an incidence angle θ. Modified from Chan and Koo (2008).

SAR imaging spatial resolution depends on the effective length of the pulse in the slant range direction and the length of the antenna in the azimuth direction. SAR satellites uses forward motion to synthesize a longer antenna aperture, this can be achieved by recording different echoes of the same object and combined them into a virtual high-resolution image (Chan and Koo, 2008).

Radar satellites do not collect images on the nadir track, they use a side look angle perpendicular to the along track. The distance between the sensor and the point where the signal is backscattered is called slant range. The smaller the slant range the greater the resolution. The acquisition of the signal works in an across track mode, where several backscatter signals are received across track, and then combined for the composition of the image in slant range. The image then needs to be ground projected creating a ground

range image. Figure 2.4 shows a simplified SAR acquisition geometry. Because of the side-looking characteristic of SAR image acquisitions, there are three types of distortion effects: foreshortening, layover and shadowing. Foreshortening occurs when the signal from the base of the mountain reaches the sensor first than the peak of the mountain, creating an effect of compression of the mountain slope. Layover on the contrary, is when the reflected signal of a mountain peak hits the sensor before the mountain base reflection, creating a sensation of a fallen mountain with the point towards the sensor. Shadowing happens when a mountain or a large object has a greater shadow than the incidence angle, preventing areas to be illuminated by the sensor, resulting in black patches with no data over the image.

Other effect that occurs on SAR images is speckle. Speckle is a particular random noise that happens when the sensor is not capable to resolve individual scatters at the spatial resolution. Hence, sharp edges like crevasse formation may look granulated. In order to reduce this effect image multi-looking and filtering techniques are used (Pellikka and Rees, 2010).

Other capabilities of SAR images are its ability to use different polarization of the electric field and the use of interferometry (InSAR) technique. SAR polarization of the emitted and received electromagnetic radiation, represented in combinations of the horizontal (H) plane and the vertical (V) plane of the electromagnetic wave, with four possible combinations of emitted and received wave states, eg., HH is the horizontal emitted and horizontal received signal. Polarimetric radar antenna requires more power and a greater data channel in order to be able to received and transmit more than one polarization (Henderson and Lewis, 1998).

The second capability, is the possibility of working with the phase of the complex signal, this technique is called Interferometry. This allows to measure small terrain changes or displacements over the earth surface, based on spatial or temporal baselines. Spatial baselines depends on the delay of the transmitted pulses, on the other hand temporal

baselines assumes an identically acquisition track, which is repeated and differences on the phase would be related to changes on the terrain (Henderson and Lewis, 1998).

The use of Synthetic Aperture Radar (SAR) imagery is widely used for glaciological studies (eg., Rignot 2008; Floricioiu et al. 2009; Han and Lee 2015). Some of the most common uses on glaciology of SAR images capabilities are creating glacier velocity fields, glacier DEM and glacier facies detection, in order to track changes in time and space (Pellikka and Rees, 2010).

2.2.2 Cosmo-SkyMED

Cosmo-SkyMED is a constellation of four satellites launched by the ASI, between the years of 2007 and 2010, for military and civilian purposes. Having a four SAR satellite constellation allows to a very short revisit and response time if needed, response time of 72 hours with a revisit of 12 hours in worst case scenario. With a capability to acquire 1800 images in 24 hours. The satellite sensors have polarimetric capabilities (i.e.,. HH, VV, HV and VH acquisition configuration options) and interferometric capabilities due to the short revisit time (Covello et al., 2010).

Each satellite has a microwave high resolution synthetic aperture radar (SAR) X-band sensor operating at $9.6\,\mathrm{GHz}$, with right and left looking capabilities and a complete orbit cycle of 16 days. They retrieve data in three different acquisition modes: Spotlight ($10\,\mathrm{km}$ area coverage and $1\,\mathrm{m}$ spatial resolution), Stripmap HIMAGE ($30\,\mathrm{km}$ area coverage and $5\,\mathrm{m}$ spatial resolution) and ScanSar ($200\,\mathrm{km}$ area coverage and $100\,\mathrm{m}$ spatial resolution). In this study, we used Stripmap HIMAGE data for surface ice velocity calculations and Spotlight-2 for glacier feature descriptions associated with surface strain rates. Between December 2011 and January 2012 four high resolution Stripmap HIMAGE and 2 Spotlight-2. Cosmo-SkyMED images were acquired (Table 2.1) taking advantage of an ASI approve project based on an announce of opportunity for scientific purposes named: "COSMO-SkyMed data in support of climate sensitivity studies of selected

glaciers in Antarctica, South America, the Arctic and Northern Europe (GlacioCOSMO)".

Figure 1.4 and 3.5 show the coverage extent of the acquire SAR images.

Table 2.1: Cosmo-SkyMED (CSK) SAR images used in this study.

Mode	Acquisition Date	Polarization	Pass	CSK-Satellites	Incidence Angle	Look Dir.
Stripmap	21/12/2011	VV	Descending	3	24.11 deg.	Right
Stripmap	14/01/2012	VV	Descending	1	24.01 deg.	Right
Stripmap	22/01/2012	VV	Descending	2	24.01 deg.	Right
Stripmap	30/01/2012	VV	Descending	1	24.07 deg.	Right
Spotlight-2	14/07/2011	HH	Descending	4	22.49 deg.	Right
Spotlight-2	13/07/2011	VV	Descending	2	22.41 deg.	Right

2.2.3 TanDEM-X

TanDEM-X is a German radar mission launched by the DLR consisting of twin satellites flying in close formation. Each satellite is carrying a X-band sensor operating at a center frequency of 9.6 GHz with an incidence angle of 33°. The prime objective of the mission is generating a high accuracy world DEM. This is achieve by InSAR bistatic mode acquisition of the images, where one satellite transmitter illuminates a common footprint. Then both satellites record simultaneously the scattered signal with different temporal baselines. TanDEM-X DEM has a relative vertical accuracy of 10 m and relative vertical accuracy of 2 m with a spatial resolution of 0.4" x 0.4" (12.35 m x 12.35 m) at the equator (Krieger et al., 2007). The DEM tiles used in this study where obtained through a DLR call for proposals on December 2016, a project was approved named "TanDEM-X data in support of glacier mass balance and remote sensing studies of glaciers in Southern Patagonia and Ellsworth Mountains - Antarctica".

2.3 GPR and Glaciological Data

An observation network of 21 stakes for measurements of glacier mass balance and ice flow velocity was first establish by Rivera et al. (2014b) in 2007. This network plus
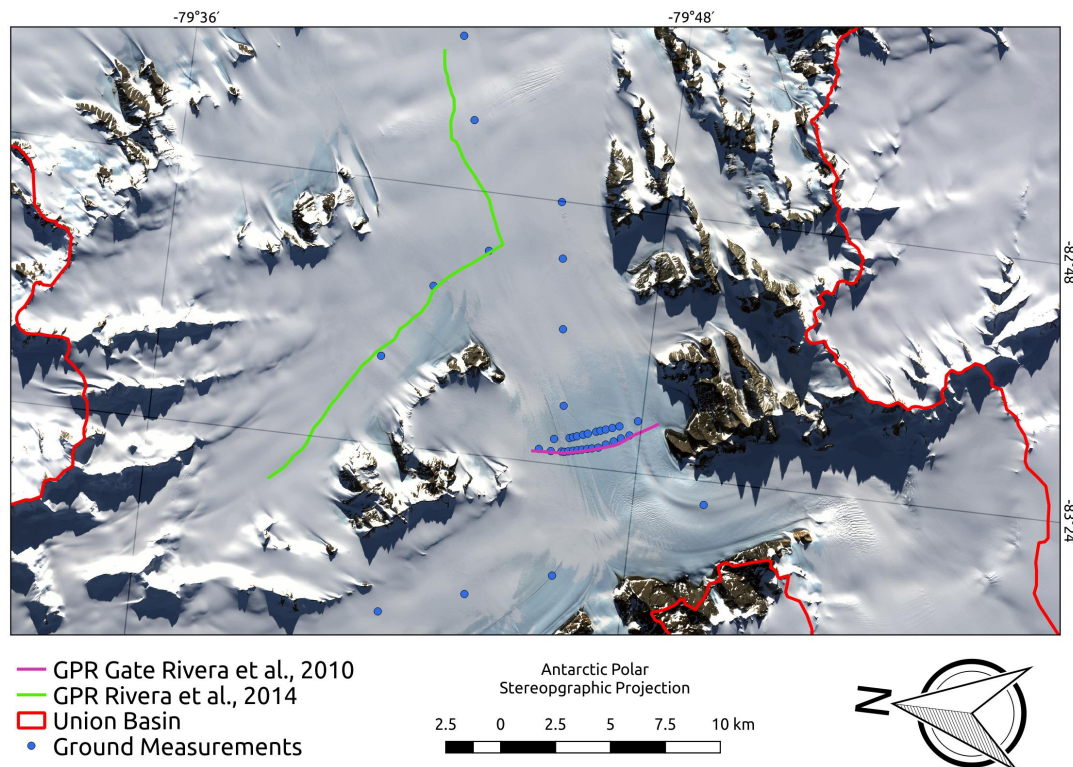
Figure 2.5: GPR and ice velocity ground data collected during different campaigns between 2008 and 2010, obtained from Rivera et al. (2014b).

35 more stakes were surveyed annually from 2008 to 2010, placement can be seen on figure 2.5. Their positions were established by GPS measurements and its displacements published by Rivera et al. (2014b). Bamboo or PVC stakes are installed on a hole in the ice drilled with a steam drill. The use of such technique is wide spread on the glaciological community as a point measurement of mass balance and glacier velocity. If they are displayed in an array they can be used to measure deformation and stress fields (eg., Nye 1959; Harper et al. 1998).

GPR data was collected between 2008 and 2010 by CECS personal, they used a coherent pulse compression radar depth sounder designed at CECS (Uribe et al., 2014) and collected more than 450 km of radar tracks along the Heritage range. We used only tracks that were over Union glacier or its tributaries, this sum up to more than 4000 GPR point measures. Some of the data was obtained from literature (Rivera et al., 2014b) and other

other was kindly made available by Andrés Rivera from CECS. The post-process was done by the CECS personal (eg., background removal, a dewow filter was applied and an adjustment of the gain function), more information can be found in Rivera et al. (2010) and Uribe et al. (2014). The data was used to calibrate and validate the ice thickness model.

Chapter 3

Methods

In this section, we present the methods for extraction of surface ice displacement, generation of an ice thickness model based on lamellar flow and calculation of principal axes surface strain rates derived from ice flow velocities.

3.1   Surface Ice Velocities

Calculation of surface ice displacement with SAR data can be done using three different methods: SAR interferometry (InSAR), offset/feature tracking, and speckle/coherence tracking (Pellika and Rees, 2010). We carried out an offset tracking procedure implemented by GAMMA Sar software, in order to estimate surface ice displacements and velocities (Werner et al., 2000). This technique has been used in several surface ice velocity studies (eg., Ciappa et al. 2010; Muto and Furuya 2013; Riveros et al. 2013; Falk et al. 2016; Satyabala 2016).

3.1.1   Offset Tracking

Offset tracking technique, sometimes called feature tracking (Pellikka and Rees, 2010), is based on a cross correlation algorithm used to infer feature displacements between pairs of images of the same location, acquired in different time frames. This technique can be performed over optical or SAR satellite images, because it depends on the ability to relate

features statistically similar in both images. We use a commercially available GAMMA
SAR software that has a offset tracking capabilities for SAR images. This technique was
selected over interferometry or coherence tracking due to the time acquisitions periods
between images (Strozzi et al., 2002).

Two satellite images of the same area acquired with the same geometry but at different
times are used as input. Time period between image acquisitions depends on the expected
surface ice velocity. If the glacier flows to slow, it is difficult to measure a displacement
between features in case of short time spans On the other hand, if the glacier ice velocity
is high, it might be difficult to maintain coherence over the images. Hence, the period of
the selected images depends on the characteristic of the studied glacier.
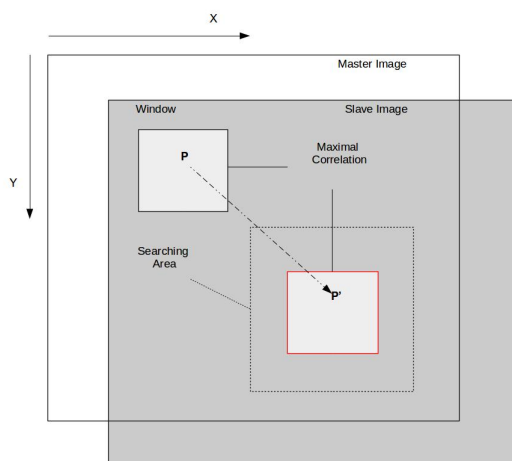
Figure 3.1: Schematic of intensity cross-correlation elements: Co-register master and
slave images. Window patches on master and slave. Search area over slave. When max-
imum cross-correlation between of master window over the search area is achieve, an
offset displacement vector $\vec{PP'}$ is inferred. Modified from Huang and Li (2009)

We followed the standard offset tracking procedure indicated for glaciological stud-
ies by the developers of the GAMMA SAR software. This procedure consists on several
different programs that need to be tuned for different image settings. The input of the
algorithm are the master and slave images in the original file formats used by the space
agencies that are providing the data. GAMMA SAR routines can be computational inten-
sive when high resolution images are used. The routine and the set parameters of each

program can be consulted on additional informations A.1.

The processing chain of the algorithm is as follows: first of all, images need to be coregistered and adjusted with precise orbit parameters, in order to reduce positioning errors between similar features found in the pair of images. All preprocessing of the SAR images if needed is done internally the software. Then, the normalized cross-correlation algorithm of SAR intensity values is performed. The data is normalized in order to smooth intensity values, this is done by subtracting the mean and divided by the standard deviation. The algorithm main idea is to define a search window over which a patch of pixels of the master image are correlated on the slave. The search process generates a cross correlation function for the image patch and the offset, defined as the maximum peak cross-correlation between the intensity patches (Figure 3.1). If near identical features exist in the images, intensity tracking can be done with high accuracy. Signal to noise ratio (SNR) between the height of the correlation peak and the mean of the correlation function is used as a threshold method. The precise estimations of the offsets are then transformed in displacements vectors (Werner et al., 2000; Strozzi et al., 2002).

The definition of the size in pixels for the search window and the intensity patch in the master image depends on the spatial resolution of the image, the expected ice displacement and the size of the surface features. Sometimes this can be a trial and error search, for the best window/patch combination. The patch size used in this study for each pair is presented on table 3.1.

Because the GAMMA SAR offset tracking algorithm results are on slant-range/azimuth geometry they need to be terrain corrected. Terrain correction process allows to convert slant-range to ground range. In such a way that can correct layover or foreshortening effects and adjust geometric parameters.

3.1.2   Geocoding of the results

Results are then terrain corrected and geo-located in order to be properly displayed and used on a GIS software. To accomplished this, a digital elevation model (DEM) must be used. We used a similar spatial resolution DEM generated by the TanDEM-X DLR mission (details on sub section 2.2.3. First step, is the creation of a parameter file that would define the appropriate projection during DEM transformation. Next step is to create look-up table that relates map coordinates with a simulated SAR image created using the DEM and the SAR orbit coordinates. The simulated SAR image in map coordinates is then resampled from map to SAR geometry and then a fine registration between the simulated intensity image and the real SAR image is accomplished and a new precise look-up table is generated. With the new look-up table the SAR image is resampled into map coordinates (AG, 2013). The Geocoding process steps are shown on figure 3.2. The Geocoding process is done with the GAMMA SAR software and the routine can be found in additional information A.2.
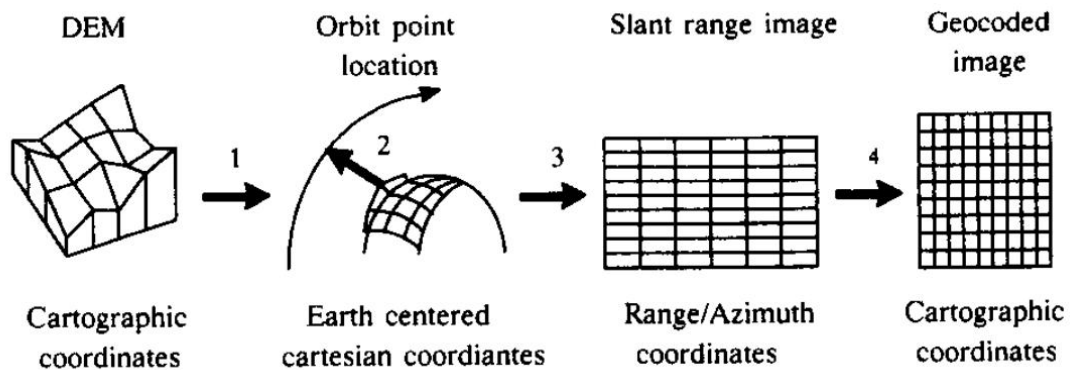
Figure 3.2: Geocoding steps with terrain correction: 1) DEM coordinate transformation; 2) Precise orbit location; 3) Transformation of slant-range values to range and azimuth coordinates; and 4) resampling into geocoded output. Modified from Bayer et al. (1991)

3.1.3 Signal to noise ratio

Signal to noise ratio (SNR) of the height of the correlation peak relative to the average level of the correlation function is established as a quality control of the offsets (Strozzi et al., 2002). We set the SNR threshold at 4.0 as recommended by previous studies (Vijay and Braun, 2017; Rankl et al., 2017). Offset results are then multi-looked and terrain corrected with high resolution Tandem-X DEM (Wegmuller et al., 1998; Strozzi et al., 2002). The results obtained from the algorithm are magnitude, ground-range and azimuth components of the velocities (e.g., velocities magnitude shown on Figure 4.1).

3.1.4 Uncertainties on surface velocity measurements

The main uncertainties in the surface velocity measurements can be associated with errors on the co-registration or related to the tracking algorithm. We follow a method, used by McNabb et al. (2012); Rankl et al. (2017); Vijay and Braun (2017), for the calculation of the uncertainties associated with the offset tracking procedure denoted as e_t at equation 3.1.

$$e_t = \frac{C\Delta x}{z\Delta t},$$

(3.1)

Where C is the error associated with the tracking algorithm (in pixels), Δx pixel resolution in ground range ($12m$), z would be the oversampling factor, we used 5 as is the multi-look parameter that gives roughly square pixels for Cosmo-SkyMED images, and Δt time amidst acquisitions. Results of e_t for each pair are presented in table 3.1. Errors associated with image co-registration were calculated by estimating RMSE velocity over stable ground.

The uncertainty calculated was plot over the image extent as a ratio of the offset tracking results. Lower velocities have greater uncertainties than higher velocities, this is the case for mountain areas, Shanz, Driscoll valleys and the area closer to the grounding line

Table 3.1: Offset tracking parameter settings and error estimations

Pair	Master	Slave	Patch Size[a]	Patch Size (m)[b]	Step[c]	Interval	RSME	e_t
Pair1	14/01/2012	30/01/2012	256x256	250x479	5/5	16 d	0.03 md^{-1}	0.07 md^{-1}
Pair2	21/12/2011	22/01/2012	512x512	499x958	30/30	32 d	0.01 md^{-1}	0.03 md^{-1}

[a]Patch size in range x azimuth (pixels).
[b]In meters approximately.
[c]Step in range/azimuth (pixels).

(Figure 3.3a), on this figure higher values are related to areas with greater percentage of velocity uncertainty.

Abs. percentage of error over Pair 1 [ln%]

-3   -2   -1   0   1   2   3

Pair 1 Ice velocities [m/d]

0   0.05   0.1   0.15   >0.2
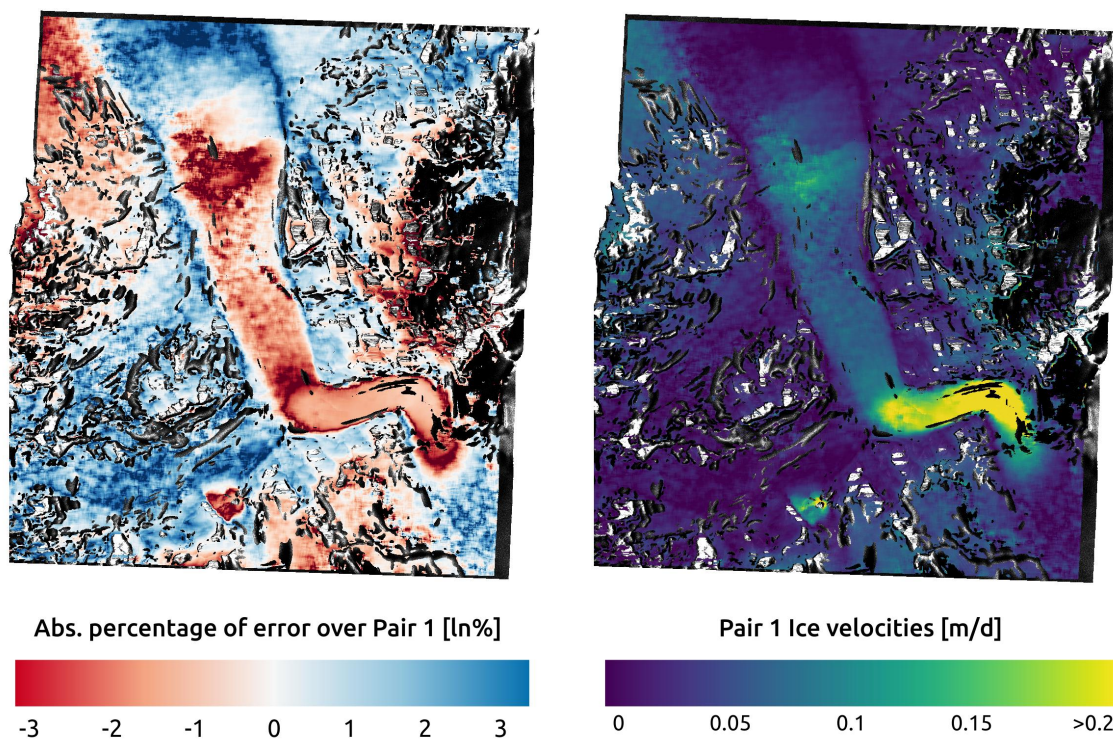
Figure 3.3: a) Percentage of the Offset tracking uncertainties over the pixel velocity, scale is in natural logarithm. Where the value 0 is when the pixel has the same value as the error; hence positive numbers are velocities lower than the estimated uncertainties and positive numbers velocities higher than the uncertainties. b) Pair 1 ice velocities in meters per day

3.2   Ice Thickness

Farinotti et al. (2017) categorize different approaches for estimating ice thickness

in five main types: (1) Minimization approach, ice thickness as an inversion problem; (2) based on Mass Conservation; (3) shear-stress-based approach; (4) velocity-based approach; (5) other approaches, for example using neural networks. We used a velocity-based approach that assumes a lamellar flow over the glacier thickness. This is also a model that after some variable assumptions needs only two inputs that vary along the glacier extend, surface velocity and slope. We already have the calculated surface velocities and slope can be derivate from the high resolution DEM obtained from TanDEM-X.

3.2.1 Lamellar Flow Model

We used a method that has been tested for glaciers in the Himalayas and the Alps (Gantayat et al., 2014; Farinotti et al., 2017) and it is based on the assumption of laminar flow (equation 3.2) (Nye, 1952b; Cuffey and Paterson, 2010; Van der Veen, 2013):

$$U_s = U_b + \frac{2A}{n+1}\tau_b^n H, \tag{3.2}$$

Where U_s refers as the surface velocity, U_b as the basal velocity, A is the flow parameter, which is assumed to be 1.2×10^{-25} s^{-1} Pa^{-3} for ice at $-20\,°C$ (Cuffey and Paterson, 2010), n is Glen's law exponential parameter set to 3 (Cuffey and Paterson, 2010), τ_b is basal drag and H ice thickness. Some assumptions are needed to be made. First, basal velocity is set to $U_b = 0$, based on Rivera et al. (2010). We can use the following relation $\tau_b = f\tau_d$ (Cuffey and Paterson, 2010), were f is defined as the shape factor related to the geometry of the valley. In this way a connection between basal and driving stresses can be made. Normally, f is considered between $[0-1]$, where 1 is infinite wide and 0 is infinite depth (Nye, 1965; Van der Veen, 2013). The shape factor can be calculated either by the center line velocities or by the balance forces acting on the glacier. Nye 1965 gives values of f for different shapes using the center line method. We decided to use this as a base and then calibrate the model (Farinotti et al., 2009) with a cross valley GPR transect at

the gate (Rivera et al., 2010). Figure 2.5 shows the GPR transect. Figure 3.4 shows the values at the transect from different sources including ones modeled in this study. Using this approach, we set f as 0.99. Then with this value we can calculate basal shear stress τ_b as (Hooke, 2005; Benn et al., 2010):
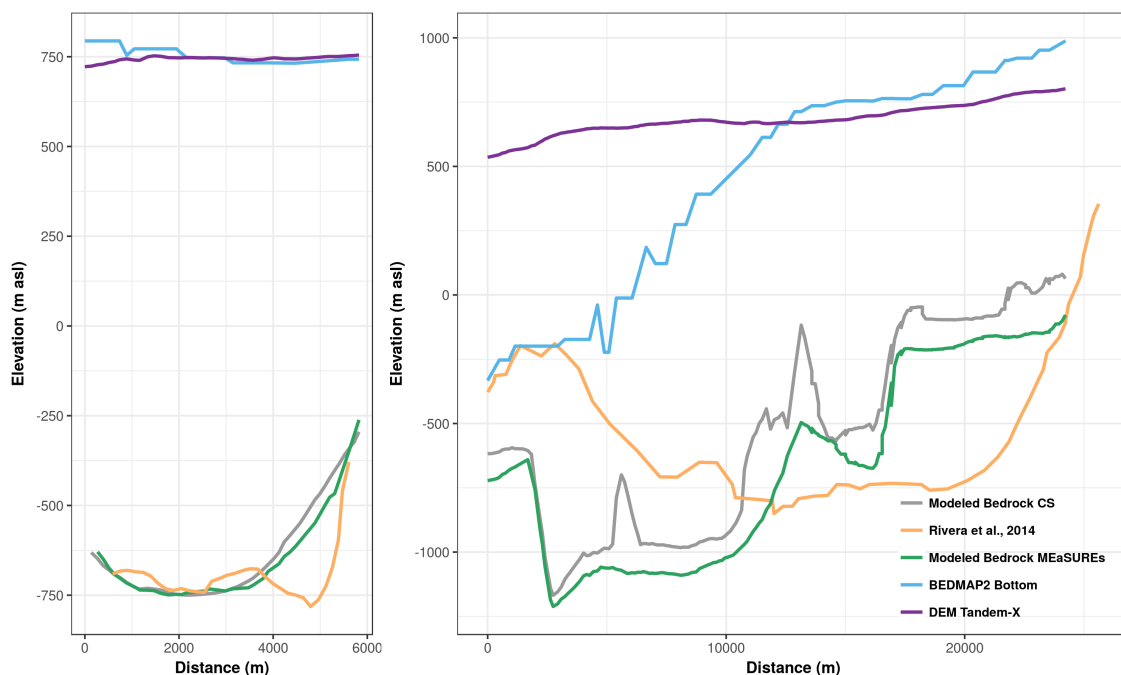
Figure 3.4: Profiles of the ice surface and bedrock of Union Glacier. GPR data set used to calibrate ice thickness model is shown in orange. Also the bedrock derived with different ice velocity sources Cosmo-SkyMED (grey) and MEaSUREs (green) using Tandem-X DEM as surface reference. Bedmap2 bedrock is also shown for comparison. Tandem-X DEM is plotted in purple.

$$\tau_b = f\rho g H \tan\alpha, \tag{3.3}$$

Where $\rho = 917\,\mathrm{kg\,m^{-3}}$, $g = 9.8\,\mathrm{m\,s^{-1}}$ and α the slope derived from TanDEM-X digital elevation model (DEM). In order to reduce the effect of longitudinal stresses, the DEM was resample to a coarser resolution using the median (Kamb and Echelmeyer, 1986; Farinotti et al., 2009; Gantayat et al., 2014). The resulting DEM was smoothed with a 9x9 window filter. The median of the slope obtained between every 100 m elevation contour was used for our purpose. Using equations 3.2 and 3.3 we find:

$$H = \sqrt[4]{\frac{2(U_s - U_b)}{Af^3(\rho g \tan \alpha)^3}}, \qquad (3.4)$$

Before applying equation 3.4 to Union glacier basin, the glacier outline is digitalized down to the grounding line using a high resolution TanDEM-X slope and the ice flow field generated from ice surface displacements complemented with MEaSUREs data. Then, the surface velocities are estimated with a spatial resolution of 100x100 m. Finally, ice thickness is calculated for the glacier outline inside the Cosmo-SkyMED extent with a 100x100 m pixel spacing, which is further smoothed using a 9x9 window median filter.

3.2.2   Uncertainties on Ice Thickness estimations

The parameters used in equation 3.4 are the source of uncertainties in the ice thickness estimation (Farinotti et al., 2009), which can be expressed, by differentiating the equation 3.4 (Gantayat et al., 2014):

$$\frac{dH}{H} = \frac{1}{4}\left[\frac{dU_s}{U_s} - \frac{dA}{A} - \frac{df}{f} - \frac{d\rho}{\rho} - \frac{d\tan\alpha}{\tan\alpha}\right], \qquad (3.5)$$

The values are defined as follows: (i) we already resolved uncertainties in U_s associated with errors in co-registration and tracking algorithm in section 3.1. Following Rivera et al. (2010), U_b was set at zero, but in order to assess the influence of the parameter, we performed a sensitivity analysis on two different sections, one over the fastest part of the glacier and the other over the main valley (section 4.2.1); (ii) The flow factor or creep parameter A over a glacier depends primarily on the variability of ice temperature, grain size, pressure, density, water content and impurities along the glacier. In order to express inherent uncertainties (dA) we will use the difference between Rivera et al. (2010) chosen value for the investigated area and ours taken from the literature (Cuffey and Paterson, 2010); (iii) Due to the fact that we used the shape factor f to adjust our model, there are three sources of uncertainties that f accounts for (Farinotti et al., 2009): approximation

of the shear stress (Nye, 1965), the distribution of basal drag across the profile (Van der Veen, 2013) and any rate of basal sliding that would be concealed within this factor. At the gate transect that we use for calibration, the mean absolute error is 90.8 m giving an error of 6% for the gate, and we set df as 0.1 following Gantayat et al. (2014); (iv) We set a 10% difference on density ρ to account for variations over the glacier profile such that $d\rho$ is set to $91.7\,\text{kg}\,\text{m}^{-3}$; (v) Uncertainties associated with slope are directly related with TanDEM-X vertical accuracy (2 m), which gives a value of 0.043 for $^{d\tan\alpha}/_{\tan\alpha}$. Putting all the values in equation 3.5 gives us an error of 16.6% in ice thickness.

3.3 Surface strain rates of Union Glacier
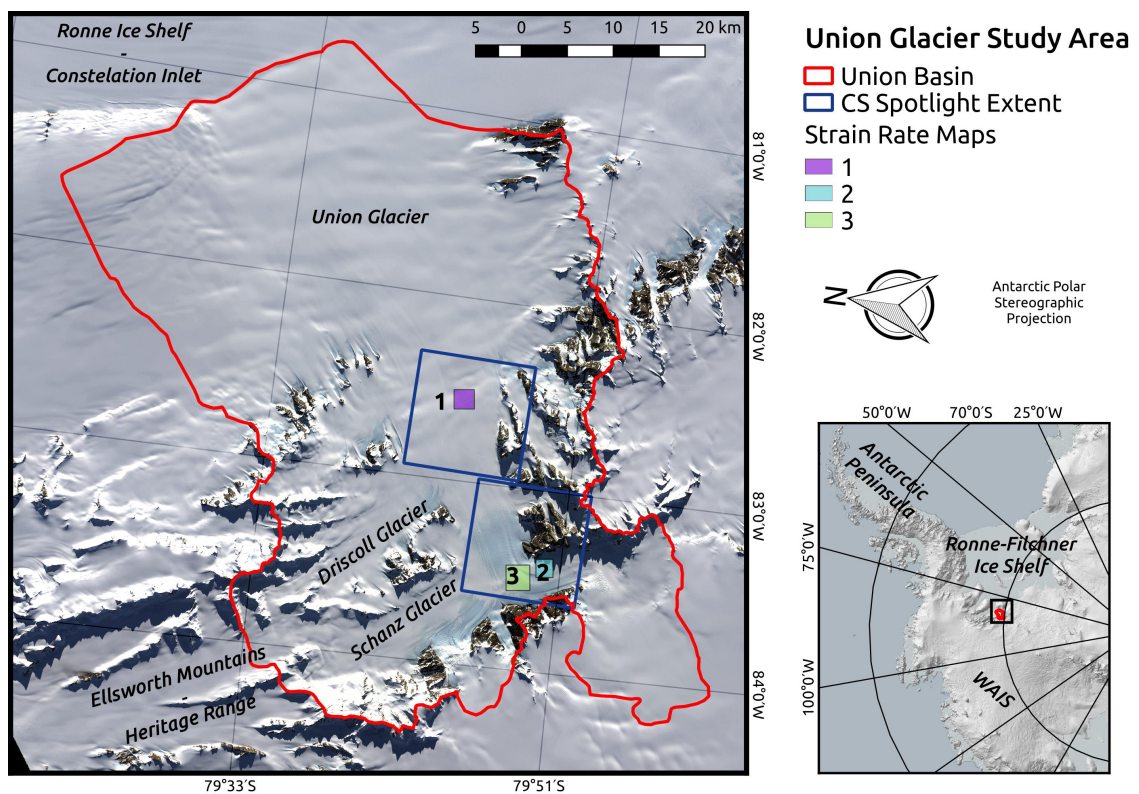
Figure 3.5: Union glacier basin with the footprints of SAR images used in the study. Blue polygons show the geographical coverages of Cosmo-SkyMED Spotlight data. Three small rectangles, indicated as 1, 2 and 3, highlight the map extents where principal strain rates were analyzed. Background image is a Landsat-8 scene in true color RGB (432) (figure 4.10, 4.11 and 4.12).

Union glacier is considered a glacier with a frozen bed (Rivera et al., 2010), meaning that it advances only by creep due to deformation of ice. Strain is the deformation of a material owing to forces applied to it. When strain is measured over a certain amount of time, it becomes a strain rate denoted by the letter $\dot{\varepsilon}$ with a dot on top (Hooke, 2005). Surface strain rate in simple shear over a glacier can be derived from surface ice velocities using the equation 3.6 , from which nine independent strains can be obtained (Harper et al., 1998; Hooke, 2005; Van der Veen, 2013). We calculated strain rates over Union glacier in a 100x100 m grid:

$$\dot{\varepsilon}_{ij} = \frac{1}{2}\left(\frac{\partial u_i}{\partial x_j} + \frac{\partial u_j}{\partial y_i}\right), \tag{3.6}$$

Using only the four components that are parallel to the glacier surface we can calculate the horizontal strain rates associated with u and v of the surface velocities over the down-glacier (x) and cross-glacier (y), following the direction of the main flux. Then, the magnitudes and direction of the least tensile $\dot{\varepsilon}_1$ and the most tensile $\dot{\varepsilon}_3$ over the horizontal xy plane are obtained:

$$\dot{\varepsilon}_1 = \frac{1}{2}(\dot{\varepsilon}_x + \dot{\varepsilon}_y) - \sqrt{\left[\frac{1}{4}(\dot{\varepsilon}_x - \dot{\varepsilon}_y)^2 + \dot{\varepsilon}_{xy}\right]} \tag{3.7a}$$

$$\dot{\varepsilon}_3 = \frac{1}{2}(\dot{\varepsilon}_x + \dot{\varepsilon}_y) + \sqrt{\left[\frac{1}{4}(\dot{\varepsilon}_x - \dot{\varepsilon}_y)^2 + \dot{\varepsilon}_{xy}\right]}, \tag{3.7b}$$

and

$$\Phi = \arctan\left(2\frac{\dot{\varepsilon}_{xy}}{\dot{\varepsilon}_x - \dot{\varepsilon}_y}\right), -\frac{\pi}{4} < \Phi < \frac{\pi}{4} \tag{3.8}$$

Where Φ relates to the angle associated with the direction between the y axis and the principal stress axes (Nye, 1959; Harper et al., 1998). Possible errors in the strain rate field calculations are closely associated with the quality of the velocity field (Rankl

et al., 2017). In order to reduce the errors, the analysis will be restricted to areas with ice movement greater than the mean flow velocity calculated over the main branch of the glacier ($\geq 0.0348\,\mathrm{m\,d^{-1}}$), following Rankl et al. (2017).

The main objective of the strain rate calculations is to relate them with surface glaciological features that can be seen over high resolution SAR Cosmo-SkyMED Spotlight-2 images and associate their formation with flow dynamics. Crevasses in SAR images can be detected as bright lines due to backscattering over rough terrain. Because of electromagnetic radiation at wavelengths used by SAR sensors is able to penetrate the snowpack, this kind of imagery shows even buried crevasses (Colgan et al., 2016). We selected three areas (figure 3.5), covered by the Spotlight-2 SAR images, which present crevasses and have velocities above than the mean ice surface velocity. Subsequently, we analyzed (1) over a longitudinal crevasse field, (2) marginal crevasses and (3) a compression zone where velocities are reduced drastically. We plotted the most and the least tensile principal strain rates in the horizontal XY plane over each area ($\dot{\varepsilon}_3$ and $\dot{\varepsilon}_1$).

Chapter 4

Results and Discussion on Union Glacier Ice Dynamics

4.1 Ice Velocities

Figure 4.1 shows the ice velocity field of Union glacier over the extent of the Cosmo-SkyMED SAR image and figure 4.1d indicates the surface ice flux direction. Maximum, mean velocities and standard deviation are obtained for the main trunk: these are $0.325\,\mathrm{m\,d^{-1}}$, $0.043\,\mathrm{m\,d^{-1}}$ and $0.0393\,\mathrm{m\,d^{-1}}$ respectively. Two pair of images were used, pair 1 (between 14 January of 2012 to 30 January of 2012) and pair 2 (between 21 December of 2011 to 22 January of 2012), in order to generate two velocity maps with almost identical results, as can be seen on figure 4.1c. The results from the longer period (32 days, pair 2 on table 3.1) showed areas with some noise (i.e., velocity outliers in figure 4.1b) over the main valley. There were attempts to improve this results choosing different window sizes over the offset tracking algorithm or changing the SNR values, but without success. The pair 2 (table 3.1) results were polluted with either noise or areas with no data, this can be noted with the difference of the two images as seen on figure 4.1c. Thus, becoming counterproductive to be used either as input for ice thickness modeling or strain rate calculations. Therefore, results from pair 1 (table 3.1) where used for ice thickness estimation and strain rates.
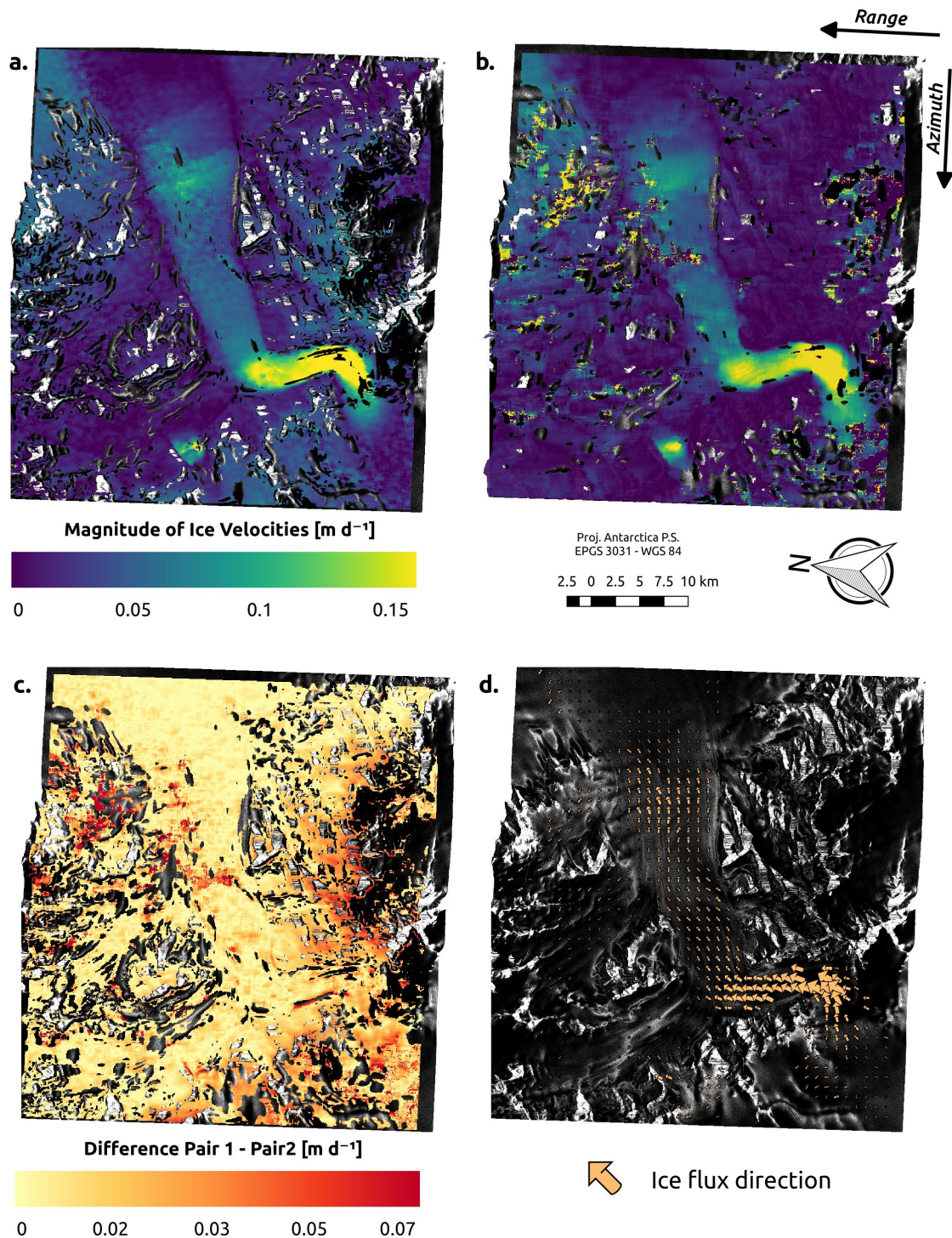
Figure 4.1: Union glacier surface velocities obtained by SAR offset tracking algorithm. a) with 16 days and b) 32 days interval between acquisitions. Brighter colors indicate higher velocities, color bar is truncated on the higher end. Larger values are observed over the more steep terrain where the ice sheet plateau connects with the valley. c) The difference between pair 1 and pair 2 in $\mathrm{m\,d^{-1}}$. and d) Main flux of the glacier with arrow scaled with the magnitude of the velocity

Table 4.1: Statistic of Surface Ice velocity over Union Glacier and its tributaries in md^{-1}.

Area	Mean	S.D.	Min	Max
1. Main Valley	0.029	0.014	0	0.114
2. Driscoll	0.025	0.020	0	0.144
3. Schanz	0.018	0.019	0	0.237
4. Plateau	0.023	0.012	0	0.084
5. Pinning Point	0.059	0.017	0.006	0.110
6. Upper Valley	0.124	0.048	0	0.316

We plot surface velocities over the center line of the glacier and compared them with changes in elevation, showing that higher velocities are associated with changes in elevation in figure 4.2. We can observe this over the area where the ice sheet flows from the plateau towards the valley, with a change in elevation of 500 m in less than 1 km (figure 4.2, approximately at 10000 m on the x coordinates). Then, the ice slows its pace when Union glacier main trunk meets its tributary Schanz glacier. This area is coincident with the main blue ice sector of the glacier. The next relative acceleration of the flow is related with the shallow ice thickness (shown by a red arrow on figure 4.6) that creates a change over the glacier elevation as seen on the 30 800 m mark over the central line transect (figure 4.2).
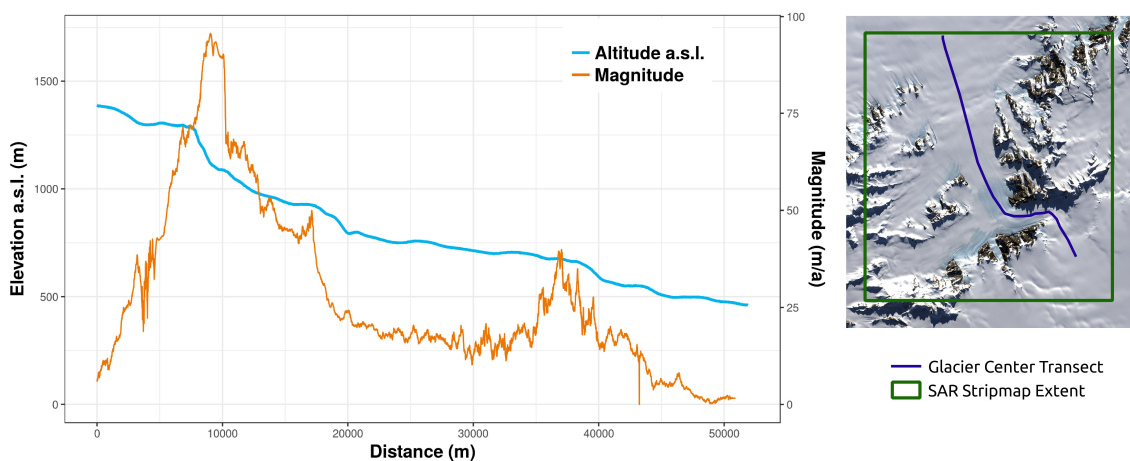
Figure 4.2: a) Union glacier center line magnitude of the velocity ($m\ d^{-1}$) profile in orange and TanDEM-X altitude (m a.s.l.) in light blue. b) Center line transect shown in blue over Landsat-8 true color image (RGB 432).

If we divide the glacier main valley in six main areas, as shown on figure 4.3a: 1) Main valley slower sections; 2) Driscoll glacier ; 3) Schanz glacier ; 4) Plateau ; 5) Pinning point ; 6) Upper Valley. Statistics of the velocities are presented on table 4.1. The upper valley velocities are one order of magnitude greater than on other areas, having also the greater standard deviation, because of the lateral drag exerted by the valley sides in this funnel section of the glacier. Even do that the area number 5, called pinning point, is the another part of the glacier where higher velocities are obtained, they just double the mean velocities of the tributaries or the slower parts of the main valley.

Driscoll glacier flows with values closer to those of the main valley slower areas. Schanz glacier on the contrary flows much slower, the high velocities are because of the ice cascade that drains some ice from the plateau.
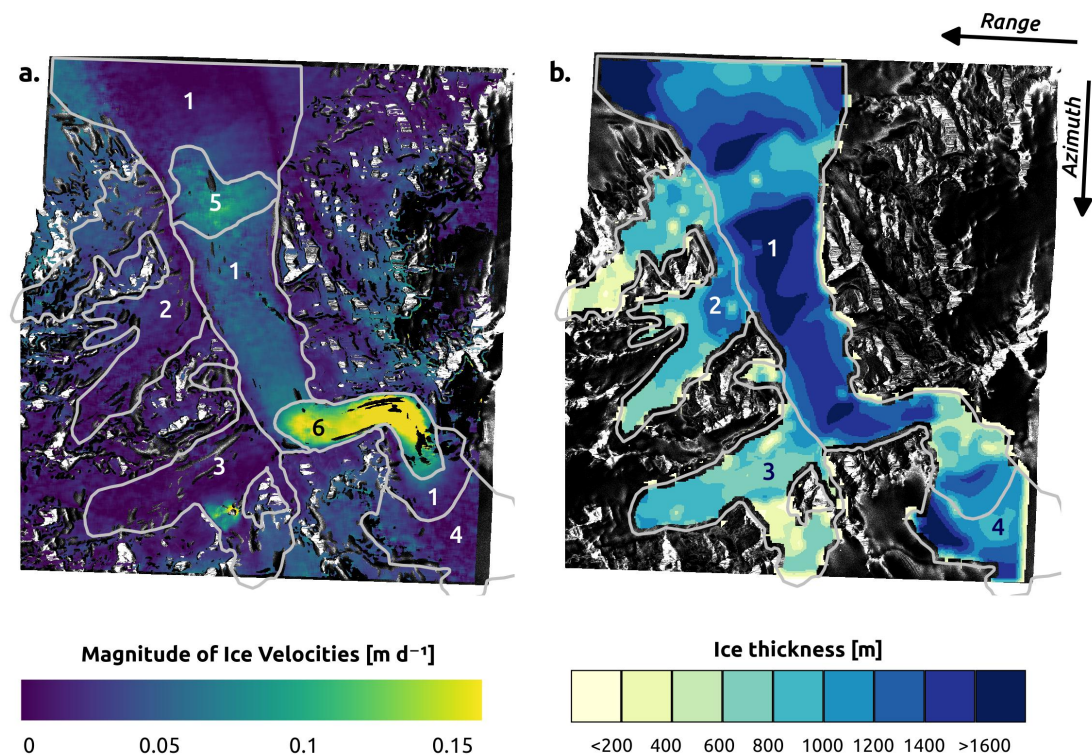
Figure 4.3: Union Glacier a) Surface ice velocity and b) Ice thickness model. With numbered areas related to statistics presented on table 4.1 and table 4.3

Glacier ice flow driven by creep is expected to have higher velocities associated with

steep terrain or abrupt changes in elevation. In the case of Union glacier, this affirmation is correct for the two areas where the velocities are higher 4.2. In the first case, when the ice flux coming from the plateau descends into Union glacier valley and in the second case over the main valley, an area where a change in elevation exists due to a rise on the bedrock. This area has been acknowledged as a pinning point of the glacier (Rivera et al., 2014b). Beside this last area, velocities over the main trunk are slower and decrease as they get closer to the grounding line because of the buttressing effect exerted by the ice shelf. This is contrary as stated by Rivera et al. (2014a) where results using sparse bamboo stakes as markers yield velocities increasing towards the grounding line. The buttressing effect is enhanced by the much faster flux of the Rutherford ice stream, that can exceed $1.2\,\mathrm{m\,d^{-1}}$ (Gudmundsson, 2006) and suppress Union glacier outlet flux. Additionally, the widening and deepening of the valley topography, after exiting the constrains of the mountain valley, helps to diminish ice velocities.

Our surface ice velocities results are in agreement with field measurements and previous studies (Rivera et al., 2010, 2014b), as shown on Table 4.2. Nonetheless, our generated velocities are compatible with the latest Antarctic Velocity map from the MEaSUREs initiative (Rignot et al., 2017). This was not the case with previous releases where a notorious difference could be seen over the upper valley area. This shows that high resolution image data sets are being used in order to construct more detailed ice velocity maps at a continental scale. The root mean square error of the differences between Cosmo-SkyMED derived velocities and field measurements is $4.298\,\mathrm{m\,a^{-1}}$ and for MEaSUREs ice velocity model is $2.744\,\mathrm{m\,a^{-1}}$, both are smaller than estimated ice velocities errors.

Even that the RSME between the ground data and the CSK and MEaSRUREs model are low a spatial difference can be seen on figure 4.4. Where almost in every point difference are below 50%, in areas of low velocities a difference of more than 180% can be noted between CSK velocity model and ground measures, point B08 on table 4.2. This difference could be explain either by the different years of the ground measures and the

Table 4.2: Comparison of field measures velocities with: Cosmo-SkyMED (CSK) derived surface velocities and MEaSUREs modeled velocities. Data is in m a^{-1} and the percentage difference at each point was calculated. GPS stations are shown in Figure 2.5 and with more detail in Figure 2 and Table 2 of Rivera et al. (2014b)

GPS Station	Longitude	Latitude	Vel. at Station	Vel. CSK	Vel. MEaSUREs	Diff. CSK (%)	Diff MEaSUREs (%)
B08	-81.965195	-79.756851	2.9	8.14212	4.733	180.763	63.207
B09	-82.453419	-79.708536	33.3	26.54531	33.04971	20.284	0.752
B10	-82.641123	-79.717176	34.6	25.73869	29.16082	25.611	15.72
B11	-82.801592	-79.756729	20.5	12.18427	19.91661	40.565	2.846
B12	-82.930014	-79.759971	20.9	21.90316	17.34298	4.8	17.019
B13	-83.090529	-79.763543	22.9	16.49623	17.18211	27.964	24.969
B14	-83.264633	-79.767491	22.4	17.90486	18.92085	20.068	15.532
B15	-83.280006	-79.798344	21.6	19.38556	18.66613	10.252	13.583
B16	-83.314627	-79.795564	23.2	20.4633	21.58851	11.796	6.946
B17	-83.34264	-79.765175	17	12.01598	14.74416	29.318	13.27
B18	-83.36934	-79.75951	14	5.38646	8.46782	61.525	39.516
B19	-83.371064	-79.764441	11.1	10.13483	12.77598	8.695	15.099
V00	-83.369388	-79.768791	18.1	12.83947	15.31552	29.064	15.384
V01	-83.369341	-79.769946	19	14.06536	15.31552	25.972	19.392
V02	-83.367162	-79.771505	20.2	16.29582	18.01662	19.328	10.809
V03	-83.364462	-79.773443	21.7	19.33093	18.01662	10.917	16.974
V04	-83.361998	-79.775219	22.3	20.83477	20.07374	6.571	9.983
V05	-83.359514	-79.777022	23	20.18964	20.07374	12.219	12.723
V06	-83.356688	-79.779086	23.5	21.60385	21.63159	8.069	7.951
V07	-83.354061	-79.781026	23.9	21.23055	21.63159	11.169	9.491
V08	-83.350741	-79.783496	24.3	22.28339	20.91835	8.299	13.916
V09	-83.341676	-79.786414	24.3	22.91436	20.99335	5.702	13.608
V10	-83.332414	-79.789416	24.3	22.71367	23.42099	6.528	3.617
V11	-83.323661	-79.792264	24	22.48447	23.48683	6.315	2.138
V12	-83.336449	-79.771399	21.9	18.18857	20.9301	16.947	4.429
V13	-83.333563	-79.77281	22.3	18.38385	20.9301	17.561	6.143
V14	-83.330481	-79.774309	22.4	18.06	23.76561	19.375	6.096
V15	-83.325526	-79.776732	22.7	17.84213	23.76561	21.4	4.694
V16	-83.321717	-79.778597	23.1	19.42115	25.90773	15.926	12.155
V17	-83.315057	-79.781881	23.4	20.61393	25.27186	11.906	7.999
V18	-83.311571	-79.783605	23.5	19.93941	25.27186	15.151	7.54
V19	-83.307388	-79.785679	23.6	20.28917	25.46391	14.029	7.898
V20	-83.302111	-79.788301	23.3	20.70112	25.46391	11.154	9.287
V21	-83.296554	-79.791081	23	20.73947	24.31866	9.828	5.733

acquisitions of the Cosmo-SkyMED images or by the time span of the samples, being the ground measures of approximately a year and CSK pair 1 of 16 days. A longer time series of ground and satellite data would be needed in order to assess the reason of the differences.
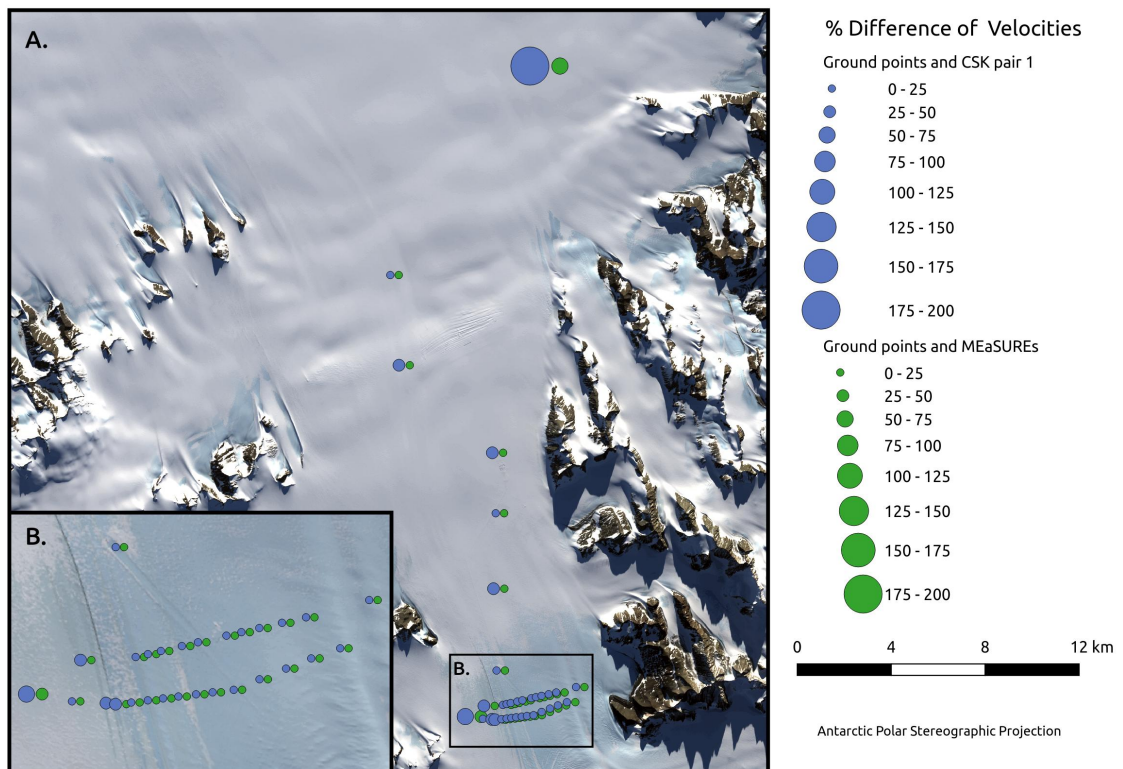
Figure 4.4: Difference between field data and CSK velocities and field data and the MEaSUREs project data (Rignot et al., 2017) in percentages.

The absolute difference between the MEaSUREs ice velocity model and the CSK pair 1 ice velocity model is presented on Figure 4.5, can be observed that the higher differences are over higher and lower velocity areas. This could be explained because of MEaSUREs uses several image pairs and filters to establish a mean velocity for each pixel, that can smooth high and low results. Also the differences are less than the calculated uncertainties for pair 1 ($0.07\,\mathrm{m\,d^{-1}}$). Hence, difference could be either explain by the MEaSUREs model or the CSK uncertainties.
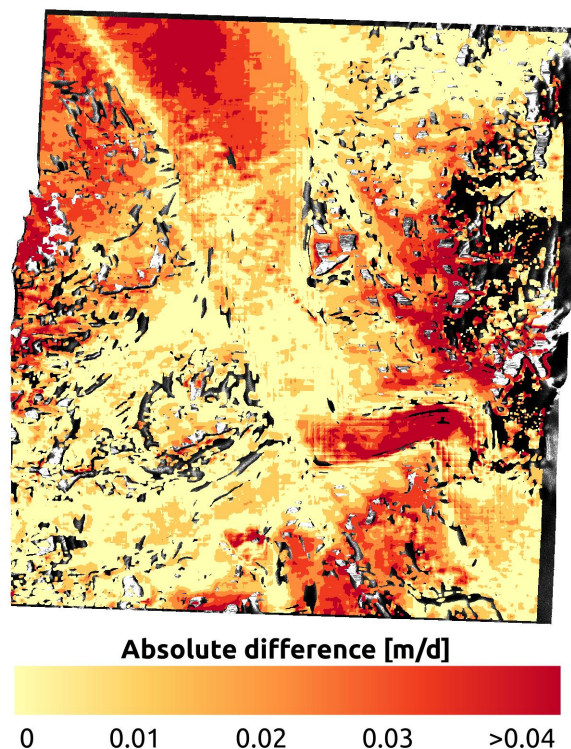
Figure 4.5: Absolute difference of the Cosmo-SkyMED ice velocity model (pair 1) and the MEaSUREs velocity data version 2 (Rignot et al., 2017) .

4.2 Ice Thickness

The ice thickness model created for Union glacier and its tributaries is shown in figure 4.6. The ice volume estimated for the glacier area covered by the extent of the SAR images is of 705.1 km^3. The deepest point of the model is 2230 m with a mean thickness of 1289.5 m for Union glacier main trunk. The values of the area identified by Rivera et al. (2014b) as the pinning point of the glacier, an indicated by a red arrow on figure 4.6 where calculated: Mean 1047.42 m; Minimum 451.09 m and Maximum 1633.94 m Ice thickness with a standard deviation of 149.59 m. This corroborates the potential future anchor point for the glacier in case of a shelf collapse.

Our results were calibrated with a GPR transect done by Rivera et al. (2010) and validated with 4107 GPR data points collected over the main valley. GPR data was acquired by Centro de Estudios Cientificos (CECS) during four different polar campaigns, with
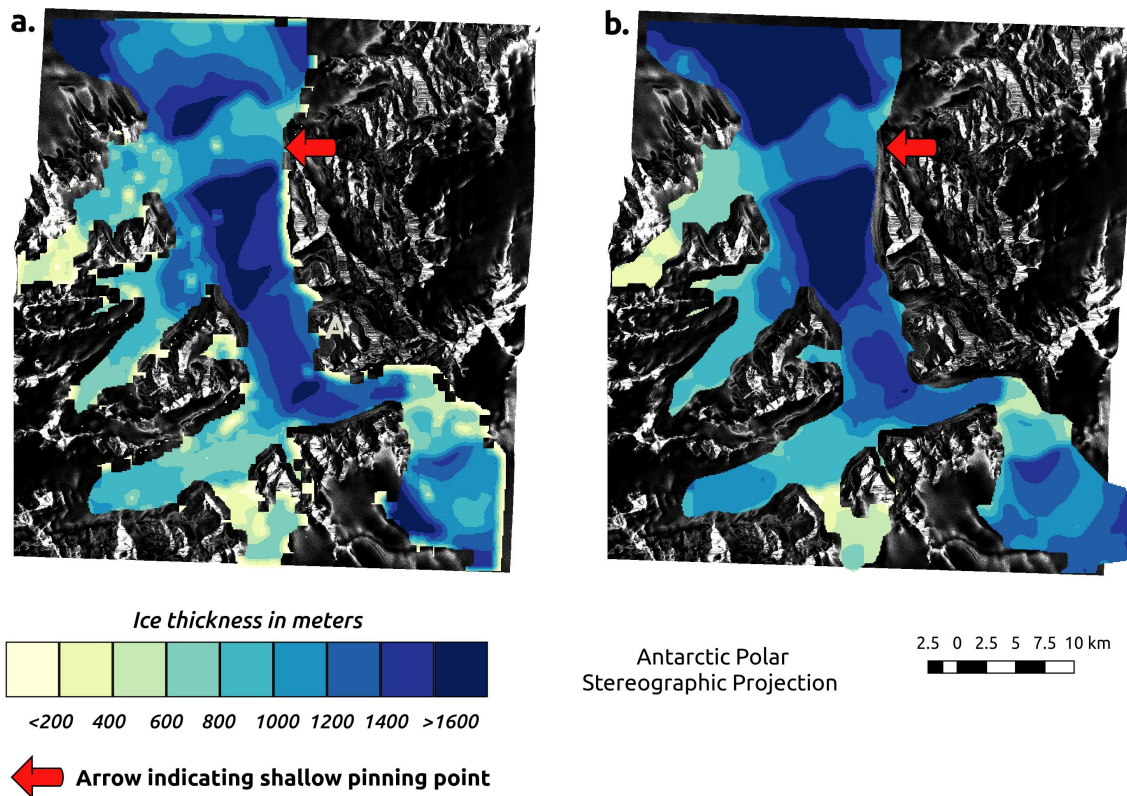
Figure 4.6: Results of the model for estimating ice thickness using different surface ice velocities from a) Cosmo-SkyMED 16 days interval and b) MEaSUREs project data (Rignot et al., 2017).

some of the data already published by Rivera et al. (2014b). In order to assess the accuracy of the model to estimate glacier ice thickness and compare it to the same model with different ice velocity input (section 4.2), we calculated average (-149.4 m), median (-183.03 m) and the interquartile range (± 315.6 m) of the difference between our model and the 4107 GPR measurements (Farinotti et al., 2017), with a mean absolute deviation of 274.42 m (21.28% of the mean model thickness) and a residual standard error of 222.7 m of our model versus the GPR measurements.

We subtracted the thickness model generated from a smooth TanDEM-X DEM surface topography in order to obtain the bedrock topography (figure 4.7). A smoothed DEM was used in order to reduce any effects of surface topographic features and trespassed to the modeled bedrock (Farinotti et al., 2009).

Table 4.3: Statistic of Ice Thickness estimations over Union Glacier and its tributaries.

Area	Mean	S.D.	Min	Max
1. Main Valley	1289.5	324.24	204.52	2230
2. Driscoll	808.3	829.3	6.3	1416.3
3. Schanz	702.3	228.08	9.15	1176.3
4. Plateau	1117.5	355.16	12.98	1680

The thickness of a cold base glacier influences directly its dynamics, with creep by deformation being is driver, and thus depending on topographic constrains of the glacier (eg. rock margins, slope, bedrock promontories). For example, the higher the slope, the thinner the glacier would be over that area (Nye, 1952a).

Bedmap-2 is a state of the art ice thickness model for the AIS (Fretwell et al., 2013). It has some differences with measured GPR data over the area of Heritage range at Ellsworth mountains (Rivera et al., 2010, 2014b). Our results also showed big differences with the Bedmap-2 model as can be seen on figure 3.4, specially over the main valley and tributaries. Thus, modeling ice thickness over mountain areas in Antarctica is of vital importance to improve estimates of ice thickness and volume.

In our case, due to the chosen value for the constant n in Glen's flow law (Glen, 1955), slope and factor f, have three times more effect over the ice thickness model, than a change in surface or basal ice velocity. In this regard, a smooth slope that represents in the best way possible the angle relative to the plane where the glacier is resting and not surface slope variations, this can be describe as a parallel-sided slab model (Cuffey and Paterson, 2010).
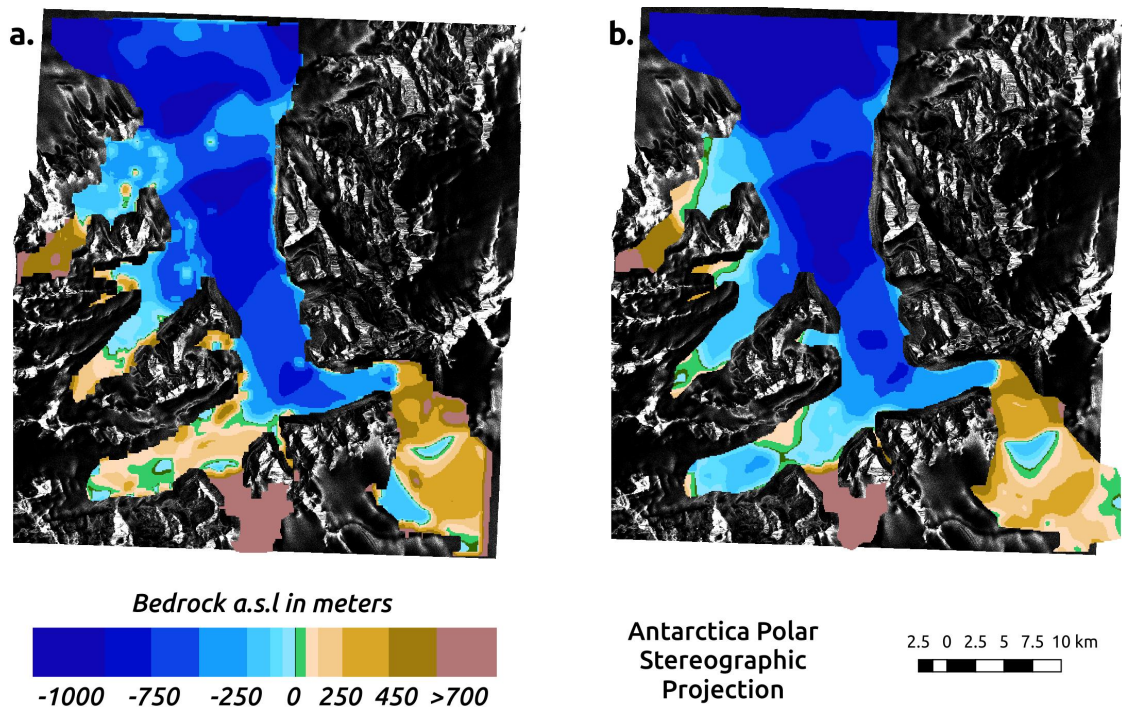
Figure 4.7: Modeled bedrock altitude of Union glacier using surface ice velocities from a) Cosmo-SkyMED 16 days interval and b) MEaSUREs project data (Rignot et al., 2017). The boundary of 0 meters a.s.l. is shown in green.

Previous GPR measurements over Union Glacier showed a shallow area that is indicated as a pinning point for the glacier (Rivera et al. (2014b)). This same area can be observed on the model (red arrow on figure 4.6) and it shows that spans over the entire width of the glacier. This means that in case of a retreat in the position of the grounding line (Ross et al., 2012), the glacier will retreat at a first stage towards this point. After that shallower area, the glacier deepens until the bedrock starts gaining elevation at the confluence of the tributaries.

The results of our model showed that the whole main glacier trunk is under sea level, under present isostatic equilibrium. This makes Union glacier sensible to a possible future Ronne-Filchner disintegration (Hellmer et al., 2012, 2017). However, if we take into consideration glacial isostatic adjustment (Watts, 2001) shallow areas (eg. pinning point, indicated by a red arrow on Figure 4.6) could end above sea level.

We also generated an ice thickness model using ice velocities from the MEaSUREs
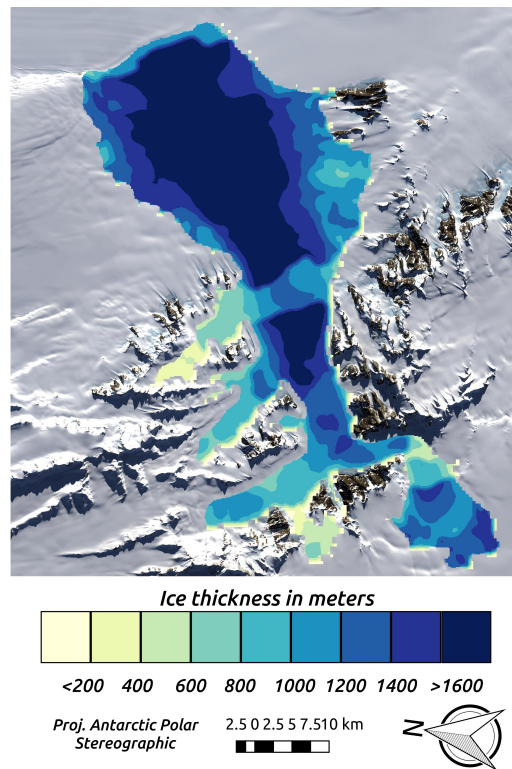
Figure 4.8: Ice thickness of Union Glacier outline using MEaSUREs surface ice velocity as input.

project (Rignot et al., 2011a). The main objective behind this was to test a high resolution velocity product with a freely available ice velocity model for the whole Antarctica. Ice thickness and sub-glacier bedrock can be seen in figures 4.6 and 4.7 respectively. In order to estimate the difference between them, we used the same parameters and validated against the 4107 GPR points. That gave us an average (-251.9 m), median (-316.9 m) and the interquartile range (± 421.4 m), then we calculated the mean absolute deviation of 317.0 m (21.43% of the mean model thickness) and a residual standard error of 219.4 m. Also a graphical comparison can be seen in figure 3.4. This comparison suggests that for a mountainous area like the Heritage range, MEaSUREs has a good representation of surface ice velocities and can be used as an input for modeling ice thickness.

Both ice thickness estimations have similar mean absolute deviations (21.28% Cosmo-SkyMED and 21.43% MEaSUREs) with respect to the GPR measurements used for

model validation, 16.6% of that difference could be explained by the uncertainties of the model. The remaining difference on ice thickness estimation, could be explained if we add the GPR uncertainties on accuracy. There area between 5% to 10% (Fischer, 2009). The error on the model reflects the inadequacy of the model to represent small changes over the bedrock because of the assumption of a parallel-sided slab model. This simplification that assumes that the surface slope is parallel to the bedrock slope induced to a poor representation of the bedrock slope between the pinning point and the valley as we can see on Figure 3.4b.

As the Cosmo-SkyMED Himage scene does not cover the whole glacier outline, from the plateau to the grounding line, and we prove that the MEaSUREs data set reflects quite well the surface ice velocity of the glacier, we use the MEaSUREs data to model the whole glacier outline ice thickness (figure 4.8). Complete estimates of glacier ice volume and sea level equivalent where obtained. The total ice volume of the define glacier outline is $1837.79\,\text{km}^3$ with a total mass of $1684.7\,\text{Gt}$, considering an ice density of $0.9167\,\text{Gt/km}^3$. Sea level equivalent was calculated taking in consideration that space occupied by the ice below sea level would not contribute to sea level rise, seawater will replace that space (Haeberli and Linsbauer, 2013). The volume of ice above sea level is $726\,\text{km}^3$ with a mass of $665.52\,\text{Gt}$. If we consider that oceans cover about 71% of the planet surface or an area of $3.62\,\text{km}^2 x 10^{-8}$, assuming an earth radius of $6370\,\text{km}$. Hence, we can calculate the volume needed to rise sea level one millimeter, and this would be $362\,\text{km}^3$. If we convert, using the relation $1\,\text{Gt}$ ice $= 1\,\text{km}^3$ water, we could assume that $362\,\text{Gt}$ would be needed to rise $1\,\text{mm}$ and sea level equivalent (SLE) can be calculated using the following relation (Cuffey and Paterson, 2010):

$$SLE = M_i \frac{1}{362} \tag{4.1}$$

Where M_i is the mass of the glacier above sea level in Gt, and $362 \pm 90.5\,\text{km}^3$ is the

volume needed to rise one millimeter of sea level. That will gave us that Union glacier has in ice a sea level equivalent of 1.84 ± 0.46 mm.

4.2.1 Ice thickness sensitivity analysis

We made a sensitivity analysis over U_b and f parameters of equation 3.2, in order to observe variations in ice thickness estimates. We did this for two different cross-profiles A-A' and B-B' (figure 4.9). We vary U_b within 10%, 20% and 30% of U_s and found that a variation of 10% does not change the results substantially, changing about 50 meters with every 10% shift in U_b , which is 5% to 3% of the total ice thickness for that section. In this respect, the existence of relative low basal velocities U_b would affect in a very small percent to the overall ice thickness and calculated volume.

However, different values of f (0.99, 0.9, 0.8, 0.7) yield a variation of more than 10% over in mean ice thickness for each section. This is similar to Farinotti et al. (2009), they found that a change of 0.1 over f (called correction factor C in their study) yielded a variation in 9% over the mean ice thickness. If using f as a calibration parameter, there should exist at least some ground data measurements in order to adjust the value, this improve results significantly.

Previous studies had shown that laminar flow model is sensitive to the f factor and A parameter chosen (Farinotti et al., 2009) and not as sensitive to changes in basal velocities (Gantayat et al., 2014).
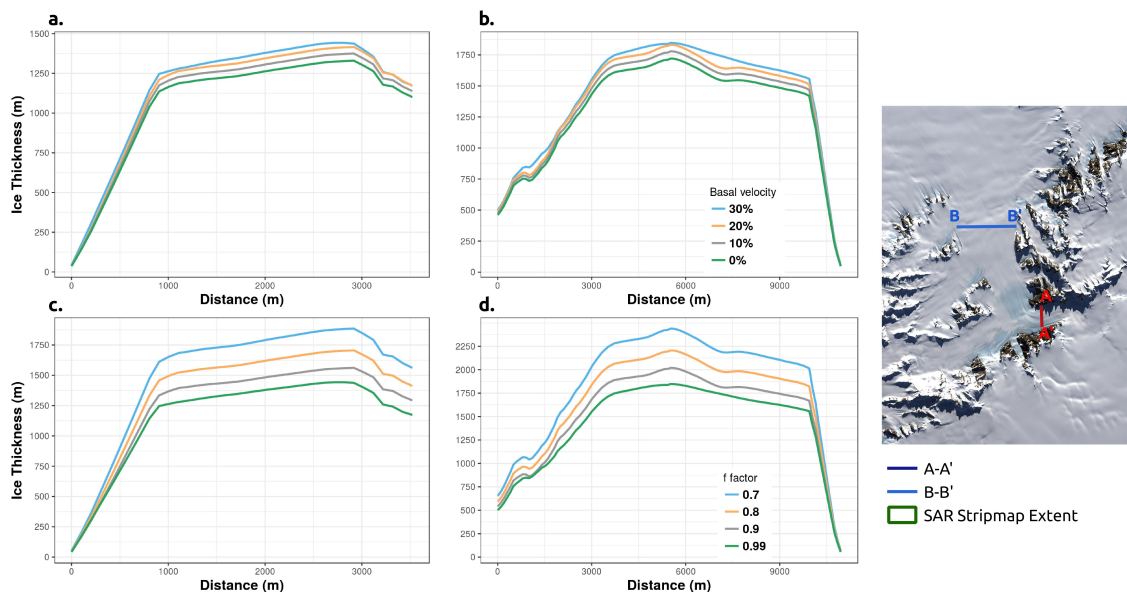
Figure 4.9: Sensibility analysis of the variations of U_b (a and b) and of f (c and d), over two cross sections of the glacier B-B' (plot a and c) and C-C' (plot b and d). Map shows position of both transects.

4.3 Strain rates

Strain rates results are presented for each selected area with a figure with two main panels, where a) shows the Cosmo-SkyMED spotlight figure with the crevasses and main ice flux direction; and b) shows the most (extension) and least (compression) strain rates axis of each area with a space resolution of 100 m.

Our results show that in general, the first area (figure 4.10), is more tensile than compressive; the second area (figure 4.11) on the contrary, shows compression as a dominant characteristic; and the third area (figure 4.12) shows significant variations between compression (negative values) and extension (positive values). The crevassed areas detected with SAR Cosmo-SkyMED Spotlight-2 images are in agreement with the crevasse fields mapped by Rivera et al. (2014a).

Figure 4.10b displays the axes of principal strain rate over the area number 1 on figure 3.5. This area is approximately of dimensions 2 x 2 km and shows a longitudinal crevasse formation and then closing, with ice surface velocities ranging between $13\,\mathrm{m\,a}^{-1}$
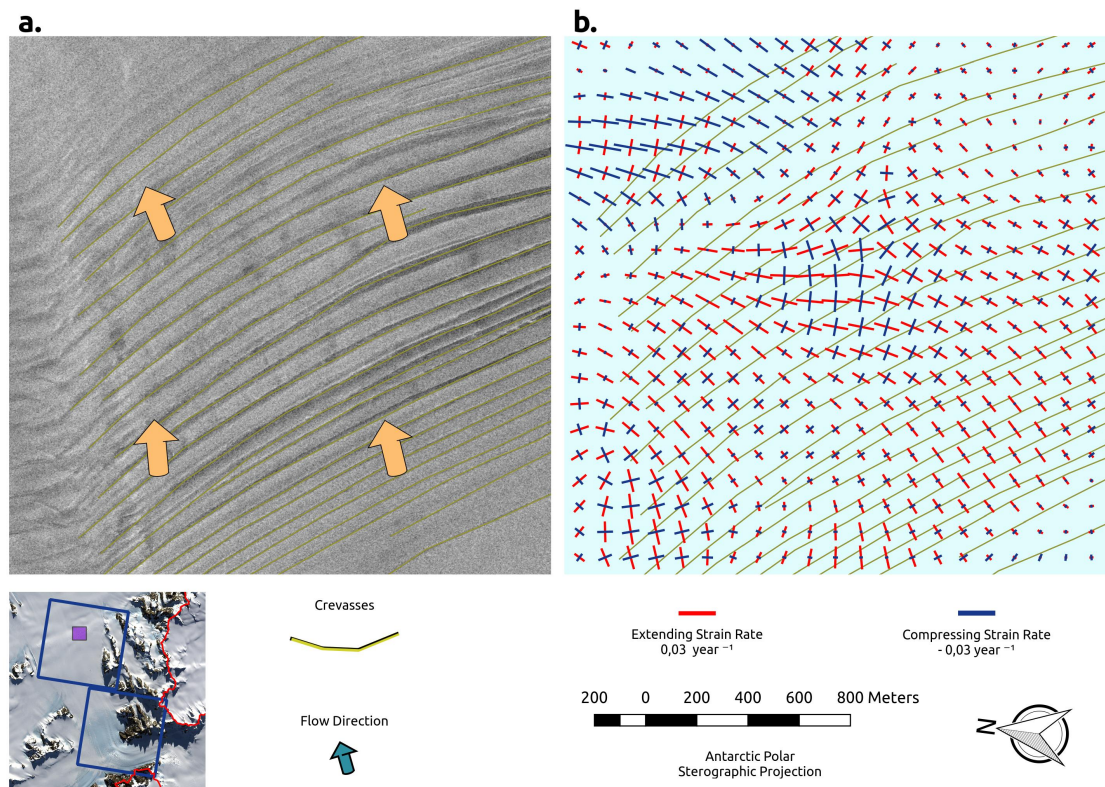
Figure 4.10: a) Enlarged area highlighting transverse crevasses over the main valley. Ice velocity magnitude (image color) and main flux direction over a Spotlight-2 image. b) Principal strain rates axes plotted over the same area, with positive tensile extension (in red) dominated the bottom of the image, an area of crevasse formation and compressive values on the top of the image where the crevasse field is closing. Values are over a 100 x 100 *m* grid. c) Map extent is shown as 1 on figure 3.5

and $39\,\mathrm{m\,a^{-1}}$. Most tensile strain-rate axes dominate the principal strain axes over the bottom and center of the area, with a compressive zone at the top of the image where crevasses are closing. Principal strain axis in extension are at a small angles to the mean flux directions, going towards the west edge of the image. Most tensile horizontal axis are at right angle with crevasses at the bottom of the image, where the generation of the crevasse field is thought to be. Longitudinal crevasses at this area are formed due to an abrupt change of bedrock topography, a shallow pinning point that acts as a barrier for the upcoming ice flow, which results in extension (bottom of the Figure 4.10). Consequently, the crevasses are generated through extending flow due to speedup of ice mass (top of the

Figure 4.10) (Hambrey and Lawson, 2000).

The principal strain rates values for this area have a maximum in extension of $22.9x10^{-3}$ a^{-1} and minimum in compression of $-1.8x10^{-2}$ a^{-1} with a compression average of $15.6x10^{-4}$ a^{-1} and a extension average of $98.5x10^{-4}$ a^{-1}.
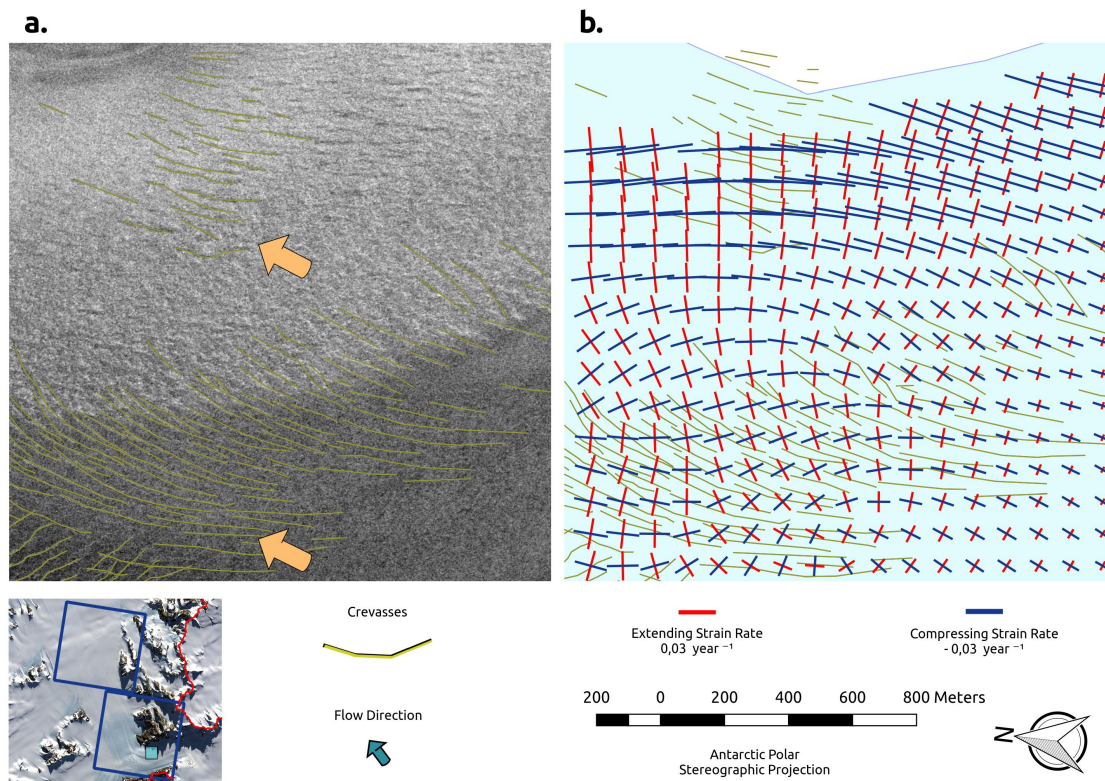
Figure 4.11: a) Enlarged area highlighting a zone with marginal crevasses and main flux direction over a Spotlight-2 image. b) Principal strain rates plotted over the same area. Values are over a 100 m x 100 m grid. Map extent is shown as 2 on figure 3.5. There is a large area with no velocity data.

Figure 4.11b display the axes of principal strain rate for area number 2, indicated in figure 3.5. This area extends over 1.6 x 1.6 km and was chosen because of the crevasses formed at the lateral margins and the strain rates associated. The area is on a mayor blue ice feature where where limited ablation occurs due to snow drift and sublimation (Bintanja, 1999; Rivera et al., 2010). In the region there is no surface melting apart from very occasional very hot summers such as the experienced in 1997 (Carrasco et al., 2000). This area consists of several marginal crevasses where compressive flux dominates and

a zone of splaying crevasses perpendicular to the main flux. The lateral stress can be observed on the magnitude of the compression of the principal axes with the most tensile principal axis normal to crevasse formation. However, the dominance of the least tensile principal axis is in accordance with the splaying crevasses formed by the compressive flux due to reduced ice surface velocity at this part of the glacier (Colgan et al., 2016).

The principal strain rates values for this area have a maximum in extension of $-37.99x10^{-3}$ a^{-1} and minimum in compression of $-7.8x10^{-2}$ a^{-1} with a compression average of $-31.7x10^{-3}$ a^{-1} and a extension average of $-19.32x10^{-3}$ a^{-1}.
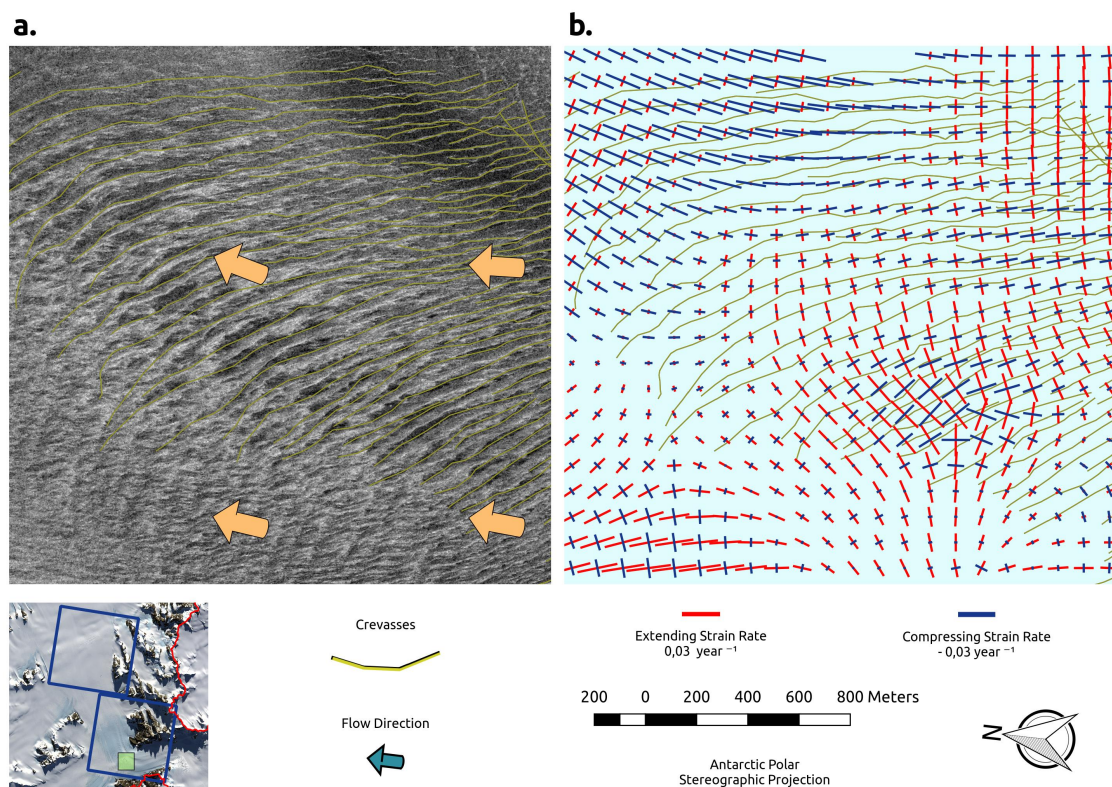
Figure 4.12: a) Enlarged area highlighting compressive flow and possible thrust-faulting area and main flux direction over a Spotlight-2 image. b) Principal strain rates plotted over the same area. Values are over a 100 m x 100 m grid. Map extent is shown as 3 on figure 3.5

Figure 4.12b displays the axes of principal strain rate for the area number 3 indicated in Figure 3.5. This area is about 2 x 2 *km* and was chosen due to the compressive flow where the fastest part of the glacier enters the main valley that is buttressed by the ice

shelf. We can observe evidence of the closure of the crevasse field as a consequence of the compressive flow, creating what looks like splaying crevasses (Colgan et al., 2016). The pattern of principal strain rates shows that the most tensile dominates up-glacier (right hand side of the image), whereas the least tensile strain rates dominate down-glacier (left hand side of the image), accordingly with the patterns of opening and closing of the crevasse field. The bottom left area that appears to be free of crevasses and has principal axes patterns that probably represent an isotropic point (Nye, 1991; Harper et al., 1998).

The principal strain rates values for this area have a maximum in extension of $39.07x10^{-3}$ a^{-1} and minimum in compression of $-40.6x10^{-3}$ a^{-1} with a compression average of $-76.6x10^{-4}$ a^{-1} and a extension average of $10.8x10^{-3}$ a^{-1}.

We relate surface principal strain rates with crevasse formation and found: a) good match between most tensile prevalence of strain rates and transverse crevasses (figure 4.10); b) change from most tensile predomination to least tensile predomination with closing of crevasses due to buttressing (figure 4.12); and c) the formation of splaying crevasses and marginal crevasses over a blue ice area (figure 4.11).

Observing the areas studied (figures 4.10, 4.11 and 4.12) it is possible to identify a low-advection life cycle (Harper et al., 1998; Colgan et al., 2016) of the analyzed crevasse fields. Hence, crevasses are being created by local stress fields in the same area where they appear, not advected from upstream stress fields (i.e., high-advection lifecycle). We can observe clear evidence of low-advection life-cycle over the crevasse field in figure 4.10. Crevasses are generated at the bottom of the image with the most tensile principal axis perpendicular to the crevasse field direction. The same area is a good example of transverse crevasses caused by a convex bed profile (pinning point) (Nye, 1952a; Colgan et al., 2016).

We could not find evidence of formation of crevasses up glacier progressing down glacier, this could be due to the topographic and glaciological constrains of Union glacier. For example, having a mild slope (average of 1.1 degree) over its main trunk and be-

ing heavily buttressed by the Ronne-Filchner ice shelf decreasing its velocity, would repress crevasse formation. Nonetheless the effect of ice buttressing and the reduction on ice velocities generates the conditions for splayed crevasses to occur in an area 60 km away from the grounding line (Figure 4.12), being an example of compressive flow (Nye, 1952a; Hooke, 2005). Compressive flow can be caused by concave bed profile, glacier bottleneck or ablation zones at the land terminus of a polythermal glacier, all of them causing horizontal velocities to diminish and vertical velocities to augment (Colgan et al., 2016).

Chapter 5

Conclusion

Using SAR offset tracking and high resolution SAR images we calculated surface ice velocities of an important area of Union glacier. We applied this results in combination with TanDEM-X to model ice thickness over the glacier and its tributaries, applying a lamellar flow model and the relation between driving stresses and basal drag. Finally we used the surface ice velocities to compute principal strain rates and relate them with glacier surface features.

Derived SAR surface ice velocities yield a maximum of $0.326\,\mathrm{m\,d^{-1}}$, a mean $0.0432\,\mathrm{m\,d^{-1}}$ with a SD of $0.0393\,\mathrm{m\,d^{-1}}$ for Union glacier, this values are in agreement with previous studies and sustains theory of a frozen bed (Rivera et al., 2010, 2014b). Areas with higher velocities are associated with strong changes in elevation, however Union glacier is heavily buttressed by the Ronne ice shelf and the Ruthford ice stream flux preventing higher velocities to occur.

The combination of different remote sensing datasets (SAR satellite imagery and GPR measurements), allow us to generate an accurate model estimation of ice thickness for the glacier. The calibration of the model with in-situ GPR measurements proof to gave us a better estimate of ice thickness. The use of MEaSUREs ice velocity dataset gave not much difference than using high-resolution SAR offset tracking on the overall ice thickness model. As estated by Farinotti et al. (2017), the use of public datasets of surface ice velocity data should be taken into advantage for future ice thickness estimations over

Antarctica. Using the MEaSUREs data set a complete ice thickness model of Union Glacier was generated, from which the total volume, mass and sea level equivalent was calculated, yielded a total of $1837.79\,\text{km}^3$, $1684.7\,\text{Gt}$ and $1.84\,\text{mm}$ respectively. The possible future effect of Union glacier, over sea level rise was quantified and an opportunity to asses the volume of the whole Heritage range opened.

The f factor combined with field measurements can be used as a calibration parameter Farinotti et al. (2009) , this will reduce significantly the model estimation error if the f value is not assumed correctly. Our results showed that variations over the f value, a relation between driving stress and basal drag, are more important than changes on basal velocity (U_b).

The ice thickness modeling approach used here does not contemplate the effects of longitudinal stresses and lateral drag over the glacier flow at a full scale, as a complete force balance equation would. Other limitations are the need of ice velocities estimates, an accurate estimation of f and A values, that in some glaciers could be hard to obtain or validate and a measure of the slope of the glacier that is a close match to the bedrock slope, herein unaffected by surface features. However, our results showed that a model based on lamellar flow is a good estimate for ice thickness, which can be used in remote areas in Antarctica.

High resolution SAR images that are in the order of $1\,\text{m}$ resolution used in association with derived products from medium resolution SAR images can be used in order to establish relations between surface features and complex ice dynamics. Over Union glacier we showed the influence of bedrock topography and ice shelf buttressing on crevasse formation. Likewise we find evidence of what we relate to low-advection crevasse lifecycle.

5.1   Recommendations for future studies

We want to finish this dissertation with some recommendations for future works over ice dynamics at this area of Antarctica. We will start with suggestions for future ice velocity studies, then ice thickness modeling and finally over ice structure dynamics.

Even do the MEaSUREs ice velocity data set have prove to be in accordance with ground measures it cant gave us a detail time series or a high resolution velocity map. In that sense future works on ice velocity should explore either high resolution or monitor seasonal or inter-annual changes over the glacier, generating time series of the glacier.

With the MEaSUREs ice velocity data set of Antarctica being constantly updated, new possibilities of Ice Dynamics modeling are opened. This data set can be used as input for modeling ice thickness, surface ice dynamics and other parameters at a medium resolution scale for remote areas of Antarctica.

With more high resolution ice velocity data for the adjacent outlet glaciers and basins (eg., Minessota, Horeshoe) strain and stress could be map and highly crevassed areas monitored. The ice thickness model should be extended for the whole Ellsworth mountain range.

Changes over grounding line migration, crevasse formation or strain rate parameters could used as proxies for the stability of the ice shelf. But a longer time series of SAR images is needed. Another option for monitoring ice shelf stability is the use of satellites with optical sensors (eg., Landsat) for assessing crevasse migration and formation.

Bibliography

AG, G. R. S., 2013. Interferometric SAR Processor - ISP. Differential Interferometry and Geocoding Software: User's guide 1.7 (July), 1–79.

Bamber, J. L., Riva, R. E. M., Vermeersen, B. L. A., LeBrocq, A. M., 2009. Reassessment of the Potential Sea-Level Rise from a Collapse of the West Antarctic Ice Sheet. Science 324 (5929), 901–903.
URL http://www.sciencemag.org/cgi/content/abstract/324/5929/901{%}5Cnhttp://www.ncbi.nlm.nih.gov/pubmed/19443778

Barahona, S., Yuivar, Y., Socias, G., Alcaíno, J., Cifuentes, V., Baeza, M., 2016. Identification and characterization of yeasts isolated from sedimentary rocks of Union Glacier at the Antarctica. Extremophiles 20 (4), 479–491.

Bayer, T., Winter, R., Schreier, G., 1991. Terrain influences in SAR backscatter and attempts to their correction. IEEE Transactions on Geoscience and Remote Sensing 29 (3), 451–462.

Benn, D. I., Evans, D. J. A., Nelson, S. A., 2010. Glaciers and Glaciation, 2nd Edition. Hodder Arnold Publication. Routledge.
URL http://www.hoddereducation.co.uk/Title/9780340905791/Glaciers{_}and{_}Glaciation{_}2nd{_}edition.htmhttps://books.google.com.br/books?id=c0xNAQAAIAAJ

Bingham, R. G., Rippin, D. M., Karlsson, N. B., Corr, H. F. J., Ferraccioli, F., Jordan, T. A., Le Brocq, A. M., Rose, K. C., Ross, N., Siegert, M. J., 2015. Ice-flow structure

and ice dynamic changes in the Weddell Sea sector of West Antarctica from radar-imaged internal layering. Journal of Geophysical Research F: Earth Surface 120 (4), 655–670.

Bintanja, R., 1999. On the glaciological, meteorological, and climatological significance of Antarctic blue ice areas. Reviews of Geophysics 37 (3), 337–359.
URL `http://doi.wiley.com/10.1029/1999RG900007`

Carrasco, J. F., Cassasa, G., Rivera, A., 2000. A warm event at Patriot Hills, Antarctica: an ENSO related phenomenon. In: Sixth International Conference on Southern Hemisphere Meteorology and Oceanography. American Meteorological Society, Boston, MA, Santiago, Chile, pp. 240–241.

Cazenave, A., Lombard, A., Llovel, W., 2008. Present-day sea level rise: A synthesis. Comptes Rendus - Geoscience 340 (11), 761–770.

Chan, Y., Koo, V., 2008. An introduction to Synthetic Aperture Radar (SAR). Progress in electromagnetic research B' 2 (6), 27–60.
URL `http://content.apa.org/reviews/008772`

Church, J., Clark, P., Cazenave, a., Gregory, J., Jevrejeva, S., Levermann, a., Merrifield, M., Milne, G., Nerem, R., Nunn, P., a.J. Payne, Pfeffer, W., Stammer, D., a.S. Unnikrishnan, 2013. Sea level change. Climate Change 2013: The Physical Science Basis. Contribution of Working Group I to the Fifth Assessment Report of the Intergovernmental Panel on Climate Change, 1137–1216.

Ciappa, A., Pietranera, L., Battazza, F., 2010. Perito Moreno Glacier (Argentina) flow estimation by COSMO SkyMed sequence of high-resolution SAR-X imagery. Remote Sensing of Environment 114 (9), 2088–2096.

Colgan, W., Rajaram, H., Abdalati, W., McCutchan, C., Mottram, R., Moussavi, M. S.,

Grigsby, S., 2016. Glacier crevasses: Observations, models, and mass balance implications. Reviews of Geophysics 54 (1), 119–161.

Cordero, R. R., Damiani, A., Ferrer, J., Jorquera, J., Tobar, M., Labbe, F., Carrasco, J., Laroze, D., 2014. UV irradiance and albedo at Union Glacier Camp (Antarctica): A case study. PLoS ONE 9 (3).

Costa, V., Vieira, R., Simões, J. C., 2017. GEOMORPHOLOGY AND SEDIMENTOLOGY OF UNION GLACIER AREA, ELLSWORTH MOUNTAINS, OCCIDENTAL ANTARCTICA. Revista Brasileira de Geomorfologia 18 (3), 103–111.
URL http://lsie.unb.br/rbg/index.php/rbg/article/view/166/288

Covello, F., Battazza, F., Coletta, A., Lopinto, E., Fiorentino, C., Pietranera, L., Valentini, G., Zoffoli, S., 2010. COSMO-SkyMed an existing opportunity for observing the Earth. Journal of Geodynamics 49 (3-4), 171–180.

Cuffey, K., Paterson, W., 2010. The Physics of Glaciers, 4th Edition. Academic Press.

Depoorter, M. A., Bamber, J. L., Griggs, J. A., Lenaerts, J. T. M., Ligtenberg, S. R. M., van den Broeke, M. R., Moholdt, G., 2013. Calving fluxes and basal melt rates of Antarctic ice shelves. Nature 502 (7469), 89–92.
URL http://www.ncbi.nlm.nih.gov/pubmed/24037377

Dutton, A., Carlson, A. E., Long, A. J., Milne, G. A., Clark, P. U., DeConto, R., Horton, B. P., Rahmstorf, S., Raymo, M. E., 2015. Sea-level rise due to polar ice-sheet mass loss during past warm periods. Science 349 (6244), aaa4019–aaa4019.
URL http://www.sciencemag.org/cgi/doi/10.1126/science.aaa4019{%}5Cnhttp://www.sciencemag.org/content/349/6244/aaa4019.abstract

Fahnestock, M., Bindschadler, R., Kwok, R., Jezek, K., 1993. Greenland Ice Sheet sur-

face properties and ice dynamics from ERS-1 SAR imagery. Science 262 (December), 1530–1534.

Fahnestock, M., Scambos, T., Moon, T., Gardner, A., Haran, T., Klinger, M., 2016. Rapid large-area mapping of ice flow using Landsat 8. Remote Sensing of Environment 185, 84–94.
URL http://dx.doi.org/10.1016/j.rse.2015.11.023

Falk, U., Gieseke, H., Kotzur, F., Braun, M., 2016. Monitoring snow and ice surfaces on King George Island, Antarctic Peninsula, with high-resolution TerraSAR-X time series. Antarctic Science 28 (02), 135–149.
URL http://www.journals.cambridge.org/abstract{_}S09541020150000577

Farinotti, D., Brinkerhoff, D. J., Clarke, G. K., Fürst, J. J., Frey, H., Gantayat, P., Gillet-Chaulet, F., Girard, C., Huss, M., Leclercq, P. W., Linsbauer, A., Machguth, H., Martin, C., Maussion, F., Morlighem, M., Mosbeux, C., Pandit, A., Portmann, A., Rabatel, A., Ramsankaran, R., Reerink, T. J., Sanchez, O., Stentoft, P. A., Singh Kumari, S., Van Pelt, W. J., Anderson, B., Benham, T., Binder, D., Dowdeswell, J. A., Fischer, A., Helfricht, K., Kutuzov, S., Lavrentiev, I., McNabb, R., Hilmar Gudmundsson, G., Li, H., Andreassen, L. M., 2017. How accurate are estimates of glacier ice thickness? Results from ITMIX, the Ice Thickness Models Intercomparison eXperiment. Cryosphere 11 (2), 949–970.

Farinotti, D., Corr, H., Gudmundsson, G. H., 2013. The ice thickness distribution of Flask Glacier, Antarctic Peninsula, determined by combining radio-echo soundings, surface velocity data and flow modelling. Annals of Glaciology 54 (63), 18–24.

Farinotti, D., Huss, M., Bauder, A., Funk, M., Truffer, M., 2009. A method to estimate ice volume and ice thickness distribution of alpine glaciers. Journal of Glaciology 55 (191), 422 – 430.

Fischer, A., 2009. Calculation of glacier volume from sparse ice-thickness data, applied to Schaufelferner, Austria. Journal of Glaciology 55 (191), 453–460.

Fitzpatrick, A. A. W., Hubbard, A., Joughin, I., Quincey, D. J., Van As, D., Mikkelsen, A. P. B., Doyle, S. H., Hasholt, B., Jones, G. A., 2013. Ice flow dynamics and surface meltwater flux at a land-terminating sector of the Greenland ice sheet. Journal of Glaciology 59 (216), 687–696.

Floricioiu, D., Eineder, M., Rott, H., Yagüe-Martinez, N., Nagler, T., 2009. Surface velocity and variations of outlet glaciers of the Patagonia Icefields by means of TerraSAR-X. In: International Geoscience and Remote Sensing Symposium (IGARSS). Vol. 2. IEEE, pp. II—-1028.

Fretwell, P., Pritchard, H. D., Vaughan, D. G., Bamber, J. L., Barrand, N. E., Bell, R., Bianchi, C., Bingham, R. G., Blankenship, D. D., Casassa, G., Catania, G., Callens, D., Conway, H., Cook, A. J., Corr, H. F., Damaske, D., Damm, V., Ferraccioli, F., Forsberg, R., Fujita, S., Gim, Y., Gogineni, P., Griggs, J. A., Hindmarsh, R. C., Holmlund, P., Holt, J. W., Jacobel, R. W., Jenkins, A., Jokat, W., Jordan, T., King, E. C., Kohler, J., Krabill, W., Riger-Kusk, M., Langley, K. A., Leitchenkov, G., Leuschen, C., Luyendyk, B. P., Matsuoka, K., Mouginot, J., Nitsche, F. O., Nogi, Y., Nost, O. A., Popov, S. V., Rignot, E., Rippin, D. M., Rivera, A., Roberts, J., Ross, N., Siegert, M. J., Smith, A. M., Steinhage, D., Studinger, M., Sun, B., Tinto, B. K., Welch, B. C., Wilson, D., Young, D. A., Xiangbin, C., Zirizzotti, A., 2013. Bedmap2: Improved ice bed, surface and thickness datasets for Antarctica. Cryosphere 7 (1), 375–393.

Gantayat, P., Kulkarni, A. V., Srinivasan, J., 2014. Estimation of ice thickness using surface velocities and slope: Case study at Gangotri Glacier, India. Journal of Glaciology 60 (220), 277–282.

Glen, J. W., 1955. The Creep of Polycrystalline Ice. Proceedings of the Royal Society of

London. Mathematical, Physical Sciences and Engineering Sciences 228 (1175), 519–538.

Gudmundsson, G. H., 2006. Fortnightly variations in the flow velocity of Rutford Ice Stream, West Antarctica. Nature 444 (7122), 1063–1064.

Haeberli, W., Linsbauer, A., 2013. Brief communication Global glacier volumes and sea level – Small but systematic effects of ice below the surface of the ocean and of new local lakes on land. Cryosphere 7 (3), 817–821.

Hambrey, M., Lawson, W., 2000. Glacier Flow and Structures. Geological Society, London, Special Publications (176), 59–83.

Han, H., Lee, H., 2015. Tide-corrected flow velocity and mass balance of Campbell Glacier Tongue, East Antarctica, derived from interferometric SAR. Remote Sensing of Environment 160, 180–192.

Harper, J. T., Humphrey, N. F., Pfeffer, W. . T., 1998. Crevasse patterns and the strain rate tensor: a high-resolution comparison. Journal of Glaciology 44 (146), 68–76.

Hellmer, H. H., Kauker, F., Timmermann, R., Determann, J., Rae, J., 2012. Twenty-first-century warming of a large Antarctic ice-shelf cavity by a redirected coastal current. Nature 485 (7397), 225–228.
URL http://www.nature.com/doifinder/10.1038/nature11064

Hellmer, H. H., Kauker, F., Timmermann, R., Hattermann, T., 2017. The fate of the Southern Weddell sea continental shelf in a warming climate. Journal of Climate 30 (12), 4337–4350.

Henderson, F., Lewis, A., 1998. Principles and applications of imaging radar. Manual of remote sensing, Volume 2, 3rd Edition. Wiley.

Hooke, R., 2005. Principles of Glacier Mechanics. Cambridge University Press.

Huang, L., Li, Z., 2009. Derivation of glacier velocity from SAR and optical data. IEEE Transactions on Geoscience and Remote Sensing, 1–2.

Jacobs, S. S., Jenkins, A., Giulivi, C. F., Dutrieux, P., 2011. Stronger ocean circulation and increased melting under Pine Island Glacier ice shelf. Nature Geoscience 4 (8), 519–523.
URL http://dx.doi.org/10.1038/ngeo1188

Joughin, I., Alley, R. B., 2011. Stability of the West Antarctic ice sheet in a warming world. Nature Geosci 4 (8), 506–513.
URL http://dx.doi.org/10.1038/ngeo1194

Kamb, B., Echelmeyer, K. A., 1986. Stress-Gradient Coupling in Glacier Flow: I. Longitudinal Averaging of the Influence of Ice Thickness and Surface Slope. Journal of Glaciology 32 (111), 267–284.
URL https://www.cambridge.org/core/product/identifier/ S0022143000015604/type/journal{_}article

Krieger, G., Moreira, A., Fiedler, H., Hajnsek, I., Werner, M., Younis, M., Zink, M., 2007. TanDEM-X: A satellite formation for high-resolution SAR interferometry. IEEE Transactions on Geoscience and Remote Sensing 45 (11), 3317–3340.

LeDoux, C. M., Hulbe, C. L., Forbes, M. P., Scambos, T. A., Alley, K., 2017. Structural provinces of the Ross Ice Shelf, Antarctica.

McNabb, R. W., Hock, R., O'Neel, S., Rasmussen, L. A., Ahn, Y., Braun, M., Conway, H., Herreid, S., Joughin, I., Pfeffer, W. T., Smith, B. E., Truffer, M., 2012. Using surface velocities to calculate ice thickness and bed topography: A case study at Columbia Glacier, Alaska, USA. Journal of Glaciology 58 (212), 1151–1164.

Mercer, J. H., 1978. West Antarctic ice sheet and CO2 greenhouse effect: a threat of disaster. Nature 271, 321–325.

Morlighem, M., Rignot, E., Seroussi, H., Larour, E., Ben Dhia, H., Aubry, D., 2011. A mass conservation approach for mapping glacier ice thickness. Geophysical Research Letters 38 (19), 1–6.

Muto, M., Furuya, M., 2013. Surface velocities and ice-front positions of eight major glaciers in the Southern Patagonian Ice Field, South America, from 2002 to 2011. Remote Sensing of Environment 139, 50–59.

Nerem, R. S., Beckley, B. D., Fasullo, J. T., Hamlington, B. D., Masters, D., Mitchum, G. T., 2018. Climate-change–driven accelerated sea-level rise detected in the altimeter era. Proceedings of the National Academy of Sciences.

Nicholls, K. W., Østerhus, S., Makinson, K., Gammelsrød, T., Fahrbach, E., 2009. Ice-ocean processes over the continental shelf of the Southern Weddell Sea, Antarctica: A review. Reviews of Geophysics 47 (3).

Nye, J., 1952a. A Methods of Calculating the Thickness of the Ice-Sheets. Nature 169 (4300), 529–530.

Nye, J., 1952b. The mechanics of glacier flow. Journal of Glaciology 2 (January), 82–93.

Nye, J., 1959. A method of determining the strain rate tensor at the surface of a glacier (6), 1–11.
  URL `papers2://publication/uuid/B878F358-4570-46EB-B40A-20FF5029B09F`

Nye, J. F., 1965. The flow of a glacier in a channel of rectangular, elliptic or parabolic cross-section. J. Glaciol. 5, 661–690.

Nye, J. F., 1991. A topological approach to the strain-rate pattern of ice sheets. Journal of Glaciology 39 (131), 10–14.

Osmanoglu, B., Navarro, F. J., Hock, R., Braun, M., Corcuera, M. I., 2014. Surface ve-
    locity and mass balance of Livingston Island ice cap, Antarctica. Cryosphere 8 (5),
    1807–1823.

Pauling, A. G., Bitz, C. M., Smith, I. J., Langhorne, P. J., 2016. The response of the
    Southern Ocean and Antarctic sea ice to freshwater from ice shelves in an earth system
    model. Journal of Climate 29 (5), 1655–1672.

Pellikka, P., Rees, W. G., 2010. Remote Sensing of Glaciers. CRC Press/Balkema.
    URL   http://scholar.google.com/scholar?hl=en{&}btnG=Search{&}q=
    intitle:Remote+Sensing+of+Glaciers{#}0

Peters, L. E., Anandakrishnan, S., Holland, C. W., Horgan, H. J., Blankenship, D. D.,
    Voigt, D. E., 2008. Seismic detection of a subglacial lake near the South Pole, Antarc-
    tica. Geophysical Research Letters 35 (23), 1–5.

Poinar, K., Joughin, I., Das, S. B., Behn, M. D., Lenaerts, J. T. M., Van Den Broeke,
    M. R., 2015. Limits to future expansion of surface-melt-enhanced ice flow into the
    interior of western Greenland. Geophysical Research Letters 42 (6), 1800–1807.

Pritchard, H., Ligtenberg, S., Fricker, H., Vaughan, D., van den Broeke, M., Padman,
    L., apr 2012. Antarctic ice-sheet loss driven by basal melting of ice shelves. Nature
    484 (7395), 502–505.
    URL   http://www.nature.com/nature/journal/v484/n7395/full/
    nature10968.html

Purkey, S. G., Johnson, G. C., 2013. Antarctic bottom water warming and freshening:
    Contributions to sea level rise, ocean freshwater budgets, and global heat gain. Journal
    of Climate 26 (16), 6105–6122.

Rankl, M., Jakob Fürst, J., Humbert, A., Holger Braun, M., 2017. Dynamic changes on

the Wilkins Ice Shelf during the 2006-2009 retreat derived from satellite observations. Cryosphere 11 (3), 1199–1211.

Rignot, E., 2008. Changes in West Antarctic ice stream dynamics observed with ALOS PALSAR data. Geophysical Research Letters 35 (12), n/a—-n/a.

Rignot, E., Casassa, G., Gogineni, P., Krabill, W., Rivera, A., Thomas, R., 2004. Accelerated ice discharge from the Antarctic Peninsula following the collapse of Larsen B ice shelf. Geophysical Research Letters 31 (18).

Rignot, E., Jacobs, S., Mouginot, J., Scheuchl, B., 2013. Ice-shelf melting around Antarctica. Science 341 (6143), 266–70.
URL http://www.ncbi.nlm.nih.gov/pubmed/23765278

Rignot, E., Jacobs, S. S., 2002. Rapid bottom melting widespread near Antarctic Ice Sheet grounding lines. Science 296 (5575), 2020–2023.

Rignot, E., Mouginot, J., Scheuchl, B., 2011a. Antarctic grounding line mapping from differential satellite radar interferometry. Geophysical Research Letters 38 (10), n/a—-n/a.

Rignot, E., Mouginot, J., Scheuchl, B., 2017. MEaSUREs InSAR-based Antarctica ice velocity map.

Rignot, E., Velicogna, I., Van Den Broeke, M. R., Monaghan, A., Lenaerts, J., 2011b. Acceleration of the contribution of the Greenland and Antarctic ice sheets to sea level rise. Geophysical Research Letters 38 (5), n/a—-n/a.

Rivera, A., Cawkwell, F., Wendt, A., Zamora, R., 2014a. Mapping blue-ice areas and crevasses in West Antarctica using ASTER images, GPS, and radar measurements. In: Kargel, J. S., Leonard, G. J., Bishop, M. P., Kääb, A., Raup, B. H. (Eds.), Global Land

Ice Measurements from Space. Springer Berlin Heidelberg, Berlin, Heidelberg, Ch. 31, pp. 743–757.

Rivera, A., Zamora, R., Rada, C., Walton, J., Proctor, S., 2010. Glaciological investigations on Union Glacier, Ellsworth Mountains, West Antarctica. Annals of Glaciology 51 (55), 91–96.

Rivera, A., Zamora, R., Uribe, J. A., Jaña, R., Oberreuter, J., 2014b. Recent ice dynamic and surface mass balance of Union Glacier in the West Antarctic Ice Sheet. The Cryosphere 8 (4), 1445–1456.
URL http://www.the-cryosphere.net/8/1445/2014/

Riveros, N., Euillades, L., Euillades, P., Moreiras, S., Balbarani, S., 2013. Offset tracking procedure applied to high resolution SAR data on Viedma Glacier, Patagonian Andes, Argentina. Advances in Geosciences 35, 7–13.

Rosanova, C., Lucchitta, B., Ferrigno, J., 1998. Velocities of Thwaites Glacier and stnaller glaciers along the. Annals of Glaciology (27), 47–53.

Ross, N., Bingham, R., Corr, H. F. J., Ferraccioli, F., Jordan, T., Le Brocq, A., Rippin, D., Young, D., Blankenship, D., Siegert, M. J., 2012. Steep reverse bed slope at the grounding line of the Weddell Sea sector in West Antarctica. Nature Geoscience 5 (6), 1–4.
URL http://dx.doi.org/DOI:10.1038/NGEO1468

Satyabala, S. P., 2016. Spatiotemporal variations in surface velocity of the Gangotri glacier, Garhwal Himalaya, India: Study using synthetic aperture radar data. Remote Sensing of Environment 181, 151–161.
URL http://dx.doi.org/10.1016/j.rse.2016.03.042

Scambos, T. A., Bohlander, J. A., Shuman, C. A., Skvarca, P., 2004. Glacier acceleration

and thinning after ice shelf collapse in the Larsen B embayment, Antarctica. Geophysical Research Letters 31 (18).

Scambos, T. A., Dutkiewicz, M. J., Wilson, J. C., Bindschadler, R. A., 1992. Application of Image Cross - Correlation to the Measurement of Glacier Velocity Using Satellite Image Data. Remote Sens Environ 42, 177–186.

Schmidtko, S., Heywood, K. J., Thompson, A. F., Aoki, S., 2014. Multidecadal warming of Antarctic waters. Science 346 (6214), 1227–1231.

Schoof, C., 2007. Ice sheet grounding line dynamics: Steady states, stability, and hysteresis. Journal of Geophysical Research: Earth Surface 112 (3), 1–19.

Shepherd, A., Wingham, D., Rignot, E., 2004. Warm ocean is eroding West Antarctic Ice Sheet. Geophysical Research Letters 31 (23), 1–4.

Stocker, T.F., D. Qin, G.-K. Plattner, M. Tignor, S.K. Allen, J. Boschung, A. Nauels, Y. Xia, V. B., (eds.), P. M., 2015. Summary for Policymakers. In: Climate Change 2013: The Physical Science Basis. Contribution of Working Group I to the Fifth Assessment Report of the Intergovernmental Panel on Climate Change. CEUR Workshop Proceedings 1542, 33–36.

Strozzi, T., Luckman, A., Murray, T., Wegm??ller, U., Werner, C. L., 2002. Glacier motion estimation using SAR offset-tracking procedures. IEEE Transactions on Geoscience and Remote Sensing 40 (11), 2384–2391.
URL http://eprints.whiterose.ac.uk/747/

Turner, J., Barrand, N. E., Bracegirdle, T. J., Convey, P., Hodgson, D. A., Jarvis, M., Jenkins, A., Marshall, G., Meredith, M. P., Roscoe, H., Shanklin, J., French, J., Goosse, H., Guglielmin, M., Gutt, J., Jacobs, S., Kennicutt, M. C., Masson-Delmotte, V., Mayewski, P., Navarro, F., Robinson, S., Scambos, T., Sparrow, M., Summerhayes,

C., Speer, K., Klepikov, A., 2014. Antarctic climate change and the environment: an update. Polar Record 50 (03), 237–259.

URL   `http://journals.cambridge.org/action/displayAbstract?aid=9285525`

Uribe, J. A., Zamora, R., Gacitúa, G., Rivera, A., Ulloa, D., 2014. A low power consumption radar system for measuring ice thickness and snow/firn accumulation in Antarctica. Annals of Glaciology 55 (67), 39–48.

Van der Veen, C., 2013. Fundamental of Glacier Dynamics. CRC Press.

Vijay, S., Braun, M., 2017. Seasonal and interannual variability of Columbia Glacier, Alaska (2011-2016): Ice Velocity, Mass Flux, surface elevation and front position. Remote Sensing 9 (6), 1–18.

Watts, A., 2001. Isostasy and Flexure of the Lithosphere. Cambridge University Press, Cambridge, UK.

Wegmuller, U., Werner, C., Strozzi, T., 1998. SAR interferometric and differential interferometric processing\nchain. IGARSS '98. Sensing and Managing the Environment. 1998 IEEE International Geoscience and Remote Sensing. Symposium Proceedings. (Cat. No.98CH36174) 2 (AUGUST 1998), 1–4.

Werner, C., Wegmuller, U., Strozzi, T., Wiesmann, A., 2000. GAMMA SAR and interferometric processing software. European Space Agency, (Special Publication) ESA SP (461), 211–219.

Young, N. W., Hyland, G., 2002. Velocity and strain rates derived from InSAR analysis over the Amery Ice Shelf, East Antarctica. Annals of Glaciology 34, 228–234.

Appendix A

Additional Information

A.1 Offset Tracking Commands

```
#### master and slave files. Creation of Single Look and
   Single Look Par ##
## master slc, slc.par file generation for Master and Slave
par_CS_SLC
   CSKS1_SCS_B_HI_0B_VV_RD_SF_20120114174758_20120114174806
   .h5 20120114  #
par_CS_SLC
   CSKS1_SCS_B_HI_0B_VV_RD_SF_20120130174747_20120130174755
   .h5 20120130  #

##### Determination of the bilinear polynomial function
#### Create Offset -- Offset file generation
create_offset 20120114_VV_0B.slc.par 20120130_VV_0B.slc.par
   20120114_20120130.off 1 1 1 1 #
### Update offset file with orbit information parameters
init_offset_orbit 20120114_VV_0B.slc.par 20120130_VV_0B.slc
   .par 20120114_20120130.off #

### Offset Power -- bilinear polynomial function estimation
   of offset fields using image intensity cross
   correlation optimization
offset_pwr 20120114_VV_0B.slc 20120130_VV_0B.slc 20120114
   _VV_0B.slc.par 20120130_VV_0B.slc.par 20120114_20120130.
   off offs snr 128 128 offsets 2 32 32 0.1   #
### Offset least square estimation fit - determination of
   the bilinear registration offset polynomial using least
   squares error method.
offset_fit offs snr 20120114_20120130.off coffs coffsets
   #
```

```
# this last step can be repeated for a better fit

#### Precise Estimation of the offsets
### Offset power tracking - estimation of offset fields
   based on bilinear polynomial function found in the
   previous step
offset_pwr_tracking 20120114_VV_0B.slc 20120130_VV_0B.slc
   20120114_VV_0B.slc.par 20120130_VV_0B.slc.par 20120114
   _20120130.off offsN snrN 5 5 offsetsN 2 4.0 32 32 1
   18420 1 25080 #
#### Computation of the range and azimuth displacements
### Offset tracking - converts range and azimuth offsets
   into displacement map saved in an intermediate complex
   file.
offset_tracking offsN snrN 20120114_VV_0B.slc.par 20120114
   _20120130.off coffsN coffsetsN 2 4 1     #

#### Display the results
### Multi look of the SLC file - multi look the master
   image for displaying the results. COSMO-SkyMed SLC: 5x4
   for approximately 10 m pixel spacing
multi_look 20120114_VV_0B.slc 20120114_VV_0B.slc.par
   master_5x5.mli master.mli.par  5 5     #

### Transform the complex file to float
# 3685 is the number of range samples, depends on
   multi_look number of looks in range and azimuth
cpx_to_real coffsN ground_range 3685 0    # extracting
   ground_range
cpx_to_real coffsN azimuth 3685 1  # extracting azimuth
cpx_to_real coffsN velocity 3685 3 # extracting velocity
cpx_to_real coffsN angle 3685 4 # extracting angle

rasdt_pwr24  velocity master_5x5.mli  3685 1  1  0  1  1
   30.  1. .35 1 velocity_CS_mag_5x5.bmp # raster type *.
   bmp for quick-look

# Next step Geocoding
```

A.2 Geocoding Commands

```
###############################
##                           ##
## GAMMA Geocoding Sequence ##
##                           ##
###############################
#
# Files needed:
# SLC master multilooked at the require resolution, best
   results if resolution is # the same as DEM. With it
   corresponding par file.
# master_5x5.mli // master_5x5.mli.par
#
#DEM file and DEM par file for the area.
# DEM_Union.dem_par // DEM_Union.dem
#
# Multi look example:
# master_5x5.mli and master_5x5.mli.par from SLC
   CosmoSkymed with multilook 5 5 for approximated 10 m
   spacing
multi_look 20120114_VV_0B.slc 20120114_VV_0B.slc.par
   master_5x5.mli master.mli.par  5 5
#
## Create DEM par for the area selected

create_dem_par DEM_Union_Terra.dem_par # posting in degrees
    for TanDEM-X: -0.000111111 0.000407407


## Display DEM to visually check its coherence
disdem_par DEM_Union_Terra.tif DEM_Union_Terra.dem_par


## Swap bytes from little to big Indian
#This step is necessary if your DEM file bytes are order in
    little indian, Gamma works in Big Indian.
swap_bytes DEM_Union_Terra.tif DEM_Union_Terra_Sw.tif 2


## Display DEM to visually check its coherence
disdem_par DEM_Union_Terra_Sw.tif DEM_Union_Terra.dem_par


####GTC - Geocoding of DEM with map coordinates


### 1. Transform DEM projection
```

```
##
# Decide the projection to use EQA, UTM, PS, etc...
create_dem_par union_master_5x5.dem_par master_5x5.mli.par
   #

# Example of Parameters:
# Polar Stereographic - PS
# REAL*4 -> asked by gc_map in order to run
# -
# -
# 3685 Width
# 5018 Lines
# -12 12 posting in mt
# N 1167000.00 E 432000.00  master.mli corner coordinates
   in meters

### 2. transform projections from EQA to UTM (bicubic
   polynomial interpolation)

dem_trans DEM_Union.dem_par DEM_Union.dem union_master_5x5.
   dem_par union_master_5x5.dem 2 2 1 0 #

### 3. Generate look up table for master.mli (range looks 5
    azimuth looks 5) from SLC CosmoSky image
## Gamma Manual has suggestions for different satellite
   missions

gc_map master_5x5.mli.par - union_master_5x5.dem_par
   union_master_5x5.dem union_CS_utm.dem_par union_CS_utm.
   dem union_CS.rough.utm_to_rdc 1 1 union_CS.utm.sim_sar #

#Display the results
disdem_par union_CS_utm.dem union_CS_utm.dem_par #
dismph union_CS.rough.utm_to_rdc 7228 # 7228 width of DEM
dispwr union_CS.utm.sim_sar 7228 #

### 4. refine look up table

geocode union_CS.rough.utm_to_rdc union_CS.utm.sim_sar 7228
    union_CS.sim_sar 3685 5018 1 0 # 3685 samples of
   master.mli 5018 lines of master.mli

# Display results
dis2pwr union_CS.sim_sar master_5x5.mli 3685 3685 #
```

```
disdem_par union_CS_utm.dem union_CS_utm.dem_par #

### 5. Computation of offsets and generation of
    registration polynomial

create_diff_par master_5x5.mli.par - master.diff_par 1 #
    created with default parameters except SNR threshold,

init_offsetm master_5x5.mli union_CS.sim_sar master.
    diff_par

offset_pwrm master_5x5.mli union_CS.sim_sar master.diff_par
        offs_5x5 snr_5x5 256 256 offsets_5x5 1 32 32 4 #

offset_fitm offs_5x5 snr_5x5 master.diff_par coffs_5x5
    coffsets_5x5


offset_pwrm master_5x5.mli union_CS.sim_sar master.diff_par
        offs_5x5 snr_5x5 128 128 offsets_5x5 1 24 24 4 #

offset_fitm offs_5x5 snr_5x5 master.diff_par coffs_5x5
    coffsets_5x5

### 6. Refinament of geocoding lookup table #

gc_map_fine union_CS.rough.utm_to_rdc 7228 master.diff_par
    union_CS.utm_to_rdc 0 #

# Display the results
dismph union_CS.utm_to_rdc 7228 #

### 7. Resampling and interpolation using a geocoding look-
    up table
## The results from the offset tracking algorithm are used
    here, combined with the look up table results.

geocode_back master_5x5.mli 3685 union_CS.utm_to_rdc
    master_5x5.mli.ps 7228 7655 2 0 #
geocode_back velocity_5x5 3685 union_CS.utm_to_rdc vel_5x5.
    mli.ps 7228 7655 2 0 #
geocode_back ground_range_5x5 3685 union_CS.utm_to_rdc
    gr_5x5.mli.ps 7228 7655 2 0 #
geocode_back azimuth 3685 union_CS.utm_to_rdc az_5x5.mli.ps
```

```
   7228 7655 2 0 #
geocode_back angle 3685 union_CS.utm_to_rdc angle_5x5.mli.
   ps 7228 7655 2 0 #


### 8. Convert GAMMA results into GeoTIFF

data2geotiff union_CS_utm.dem_par master_5x5.mli.ps 2
   master_utm_5x5.tif #

data2geotiff union_CS_utm.dem_par vel_5x5.mli.ps 2
   vel_utm_5x5.tif #
data2geotiff union_CS_utm.dem_par gr_5x5.mli.ps 2
   gr_utm_5x5.tif #
data2geotiff union_CS_utm.dem_par az_5x5.mli.ps 2
   az_utm_5x5.tif #
data2geotiff union_CS_utm.dem_par angle_5x5.mli.ps 2
   angle_utm_5x5.tif #


####################################################
```

A.3   Ice Thickness R code

```
###
# Ice-thickness
#
# Using formulas as in GENTALYAL et al 2014
#
# Laminar flow (Cuffey and Paterson 2010 4ed)
# Us = Ub + (2*A/n+1)*tb^n*H
# Basal Stress (Hooke, 2005)
# tb = f*d*g*H*tan(a)
#
# Us: Surface Velocity
# Ub: Basal Velocity
# A: Flow parameter
# n: Glen's law exponential parameter
# tb: Basal stress
# H: Ice thickness
# f: Shape factor
# d: Density of ice
# g: Gravity
####
# Files needed
# DEM slope
# Surface Velocity, this example uses the MEaSUREs V2 data
   set
### Load required libraries
library(raster)

vel_100_ag <- raster("MeSUREs_v2_Union_outline_bacia.tif")
   #
vel_100 <- vel_100_ag #


slope_100_gr <- raster("slope_bacia_reclas_100_ med.tif") #
vel_100 <- resample( vel_100,slope_100_gr, method="ngb") #


# Parameters

# Flow or Creep Parameter [1/Pa3 1/s1],  Cuffey and
   Paterson 2010, pag 75
A = 1.2*10^-25 #
```

```
shape factor from Width Averaged Force balance (RECTANGULAR
    BASIN) Van der Veen 2013
#f = 0.799 # It was not used

d = 917 # density of ice 900 kg/m3 Rivera 2010
g = 9.81 # gravity m/s2

Us <- vel_100/365 # Velocity from year to day
Us <- Us/86400 #velocity to m/sec

x <- 0 # Flow by creep, basal velocities = 0

Ub <- x*Us # Ub basal velocities; Us surface velocities; x
  relation between the two

# Slope from degree to radians
slope_100_rad <- calc(slope_100_gr, fun=function(x){(x * pi
  )/180})


f=0.99 # f in this case was used as a calibration factor
  and not just as a shape factor, look Farinotti, et. al
  (2009)

# Calculation of Ice Thickness
H <-  (2*(Us-Ub)/(A*(f^3)*(d*g*tan(slope_100_rad))^3))^(1/
  4) #

# 9x9 window filter
r3_099 <- focal(H, w=matrix(1/81,nrow=9,ncol=9), na.rm=T )
  #

# Save to a raster file
writeRaster(r3_099,"thk_100_f9x9_f099_MEsUREs.tif", format=
  "GTiff", overwrite=T)
```

A.4 Ice Strain Rates R code

```
##
# Strain rates script
#
# Load libraries
library(raster)
library(sp)
library(maptools)

# path to file
az <- "azimut_ps_100_f9.tif" # Azimuth (y)
gr <- "gr_ps_100_f9.tif" # Ground range (x)

# load as raster file
ras_az <- raster(az)
ras_gr <- raster(gr)

## For this particular data set was converted to m/y and
    velocities over 120 m/y where treated as outliers

ras_az <- (ras_az/16)*365
ras_gr <- (ras_gr/16)*365
# outliers
ras_az[ras_az>120] <- NA
ras_az[ras_az<0] <- NA
ras_gr[ras_gr>120] <- NA
ras_gr[ras_gr<0] <- NA

# Aggregation using median if needed
#ras_az_100 <- aggregate(ras_az, fact=10, fun=median)
#ras_gr_100 <- aggregate(ras_gr, fact=10, fun=median)

# check dimentions
dim(ras_az)

dx =100 #pixel in meters

i <- 1:dim(ras_az)[1]
j <- 1:dim(ras_az)[2]

ux <- as.matrix(ras_gr)
uy <- as.matrix(ras_az)
```

```r
# in order to follow flux the raster must be rotated
rotate <- function(x) t(apply(x, 2, rev))
ux <- (rotate(ux))
uy <- (rotate(uy))

# creation of variables
dim_ux <- dim(ux)
dim_uy <- dim(uy)
ux <- array(data=ux, dim = dim_ux )
uy <- array(uy, dim = dim_uy)
divergence <- matrix( NA, nrow=dim_ux[1], ncol = dim_ux[2])
shear <- matrix( NA, nrow=dim_ux[1], ncol = dim_ux[2])
rotation <- matrix( NA, nrow=dim_ux[1], ncol = dim_ux[2])
strain_X <- matrix( NA, nrow=dim_ux[1], ncol = dim_ux[2])
strain_Y <- matrix( NA, nrow=dim_ux[1], ncol = dim_ux[2])

## Calculation of strain rates
a <- dim_ux[1]-1
b <- dim_ux[2]-1
i <- 3 #
j <- 3 #

for( i in 2:a) { #
  for(j in 2:b) { #

        divergence[i,j]  <-  (ux[i,j+1]-ux[i,j-1])/(2*dx) +
           (uy[i-1,j]-uy[i+1,j])/(2*dx)
        shear[i,j]  <- 1/2* ( (ux[i-1,j]-ux[i+1,j])/(2*dx)
           + (uy[i,j+1]-uy[i,j-1])/(2*dx)  )
        #rotation[i,j,1]  <- 1/2* ( (ux[i-1,j,1]-ux[i+1,j
           ,1])/(2*dx) - (uy[i,j+1,1]-uy[i,j-1,1])/(2*dx)
           )
        strain_X[i,j] <- ( (ux[i,j+1]-ux[i,j-1])/(2*dx))
        strain_Y[i,j] <- ( (uy[i-1,j]-uy[i+1,j])/(2*dx))
  }

}

# Calculation of Principal Strain Components

i <- 1 #
j <- 1 #
a <- dim_ux[1]
b <- dim_ux[2]
```

```r
theta <- matrix( NA, nrow=dim_ux[1], ncol = dim_ux[2])
raiz <- matrix( NA, nrow=dim_ux[1], ncol = dim_ux[2])
Strain_magnitude_1 <- matrix( NA, nrow=dim_ux[1], ncol =
   dim_ux[2])
Strain_magnitude_3 <-matrix( NA, nrow=dim_ux[1], ncol = dim
   _ux[2])

for( i in 1:a) { #
  for(j in 1:b) { #

    theta[i,j]  <-  (strain_X[i,j] - strain_Y[i,j] )
    theta[i,j] <- atan2(2*shear[i,j],theta[i,j])/2

    raiz[i,j] <- sqrt((0.25*((strain_X[i,j] - strain_Y[i,j]
       )^2)) + shear[i,j]^2)

    Strain_magnitude_1[i,j] <- (strain_X[i,j] + strain_Y[i,
       j] ) - raiz[i,j]
    Strain_magnitude_3[i,j] <- (strain_X[i,j] + strain_Y[i,
       j] ) + raiz[i,j]



  }

}

# Rotate to original orientation
divergence <- rotate(rotate(rotate(divergence)))
shear <- rotate(rotate(rotate(shear)))
strain_X <- rotate(rotate(rotate(strain_X)))
Strain_magnitude_3 <- rotate(rotate(rotate(Strain_magnitude
   _3)))
theta <- rotate(rotate(rotate(theta)))
Strain_magnitude_1 <- rotate(rotate(rotate(Strain_magnitude
   _1)))

# Create raster of each variable
shear_bb <- raster(shear,
                xmn=ras_az@extent@xmin,
                xmx=ras_az@extent@xmax,
                ymn=ras_az@extent@ymin,
                ymx=ras_az@extent@ymax,
                crs=CRS("+proj=stere +lat_0=90 +lat_ts=0 +
                   lon_0=0 +k=1 +x_0=0 +y_0=0 +datum=WGS84
```

```
                       ⌴+units=m⌴+no_defs⌴+ellps=WGS84⌴+
                       towgs84=0,0,0")
                   )

strain_long_b <- raster(strain_X,
                   xmn=ras_az@extent@xmin,
                   xmx=ras_az@extent@xmax,
                   ymn=ras_az@extent@ymin,
                   ymx=ras_az@extent@ymax,
                   crs=CRS("+proj=stere⌴+lat_0=90⌴+lat_ts=0⌴
                       +lon_0=0⌴+k=1⌴+x_0=0⌴+y_0=0⌴+datum=
                       WGS84⌴+units=m⌴+no_defs⌴+ellps=WGS84⌴+
                       towgs84=0,0,0")
                   )

divergence_b <- raster(divergence,
                       xmn=ras_az@extent@xmin,
                       xmx=ras_az@extent@xmax,
                       ymn=ras_az@extent@ymin,
                       ymx=ras_az@extent@ymax,
                       crs=CRS("+proj=stere⌴+lat_0=90⌴+lat_
                           ts=0⌴+lon_0=0⌴+k=1⌴+x_0=0⌴+y_0=0⌴+
                           datum=WGS84⌴+units=m⌴+no_defs⌴+
                           ellps=WGS84⌴+towgs84=0,0,0")
                       )



Strain_magnitude_1_b <- raster(Strain_magnitude_1,
                       xmn=ras_az@extent@xmin,
                       xmx=ras_az@extent@xmax,
                       ymn=ras_az@extent@ymin,
                       ymx=ras_az@extent@ymax,
                       crs=CRS("+proj=stere⌴+lat_0=90⌴+lat_
                           ts=0⌴+lon_0=0⌴+k=1⌴+x_0=0⌴+y_0=0⌴+
                           datum=WGS84⌴+units=m⌴+no_defs⌴+
                           ellps=WGS84⌴+towgs84=0,0,0")
                       )

Strain_magnitude_3_b <- raster(Strain_magnitude_3,
                           xmn=ras_az@extent@xmin,
                           xmx=ras_az@extent@xmax,
                           ymn=ras_az@extent@ymin,
                           ymx=ras_az@extent@ymax,
```

```
                                       crs=CRS("+proj=stere +lat_
                                          0=90 +lat_ts=0 +lon_0=0 +
                                          k=1 +x_0=0 +y_0=0 +datum=
                                          WGS84 +units=m +no_defs +
                                          ellps=WGS84 +towgs84
                                          =0,0,0")
                                       )


theta_b <- raster(theta,
                       xmn=ras_az@extent@xmin,
                       xmx=ras_az@extent@xmax,
                       ymn=ras_az@extent@ymin,
                       ymx=ras_az@extent@ymax,
                       crs=CRS("+proj=stere +lat_0=90 +lat_ts
                          =0 +lon_0=0 +k=1 +x_0=0 +y_0=0 +
                          datum=WGS84 +units=m +no_defs +ellps
                          =WGS84 +towgs84=0,0,0")
                       )

# Write *.tif file of the results
writeRaster(shear_bb,"shear_union_y_100_90.tif", format="
   GTiff", overwrite=T)
writeRaster(strain_long_b,"strain_long_y_100_90.tif",
   format="GTiff", overwrite=T)
writeRaster(Strain_magnitude_1_b, "Strain_magnitude_1_y_100
   _90.tif", format="GTiff", overwrite=T)
writeRaster(Strain_magnitude_3_b,"Strain_magnitude_3_y_100_
   90.tif", format="GTiff", overwrite=T)
writeRaster(theta_b,"theta_y_100_90.tif", format="GTiff",
   overwrite=T)
```